

#### **OPEN ACCESS**

EDITED BY Haruyuki Kamiya, Hokkaido University, Japan

REVIEWED BY
Simon Arthur Sharples,
Cincinnati Children's Hospital Medical Center,
United States
Hiroshi Kuba,
Nagoya University, Japan

\*CORRESPONDENCE Yaroslav I. Molkov ☑ ymolkov@gsu.edu

<sup>†</sup>These authors have contributed equally to this work

<sup>‡</sup>These authors share senior authorship

RECEIVED 22 September 2025 ACCEPTED 24 October 2025 PUBLISHED 11 November 2025

#### CITATION

Molkov YI, Krust F, Jeter R, Stell T, Mohammed MAY, Brocard F and Rybak IA (2025) Ionic mechanisms underlying bistability in spinal motoneurons: insights from a computational model. Front. Cell. Neurosci. 19:1710893. doi: 10.3389/fncel.2025.1710893

© 2025 Molkov, Krust, Jeter, Stell, Mohammed, Brocard and Rybak. This is an open-access article distributed under the terms of the Creative Commons Attribution License (CC BY). The use, distribution or reproduction in other forums is permitted, provided the original author(s) and the copyright owner(s) are credited and that the original publication in this journal is cited, in accordance with accepted academic practice. No use, distribution or reproduction is permitted which does not comply with these terms.

# Ionic mechanisms underlying bistability in spinal motoneurons: insights from a computational model

Yaroslav I. Molkov<sup>1,2\*</sup>, Florent Krust<sup>3†</sup>, Russell Jeter<sup>1,2†</sup>, Tommy Stell<sup>1</sup>, Mohammed A. Y. Mohammed<sup>1</sup>, Frédéric Brocard<sup>3‡</sup> and Ilya A. Rybak<sup>4‡</sup>

<sup>1</sup>Department of Mathematics and Statistics, Georgia State University, Atlanta, GA, United States, <sup>2</sup>Neuroscience Institute, Georgia State University, Atlanta, GA, United States, <sup>3</sup>Institut de Neurosciences de la Timone, Aix Marseille University, Centre National de la Recherche Scientifique (CNRS), Marseille, France, <sup>4</sup>Department of Neurobiology and Anatomy, Drexel University College of Medicine, Philadelphia, PA, United States

Spinal motoneurons are the final output of spinal circuits that engage skeletal muscles to generate motor behaviors. Many motoneurons exhibit bistable behavior, alternating between a quiescent resting state and a self-sustained firing mode, classically attributed to plateau potentials driven by persistent inward currents. This intrinsic property is important for normal movement control, but can become dysregulated, causing motor function deficits, like spasticity. Here we use a conductance-based single-compartment model, together with mouse spinal slice recordings, to investigate the ionic interactions underlying motoneuron bistability. We show that synergistic interactions among highvoltage-activated L-type  $Ca^{2+}$  current ( $I_{CaL}$ ), calcium-induced calcium release (CICR) and the  $Ca^{2+}$ -activated non-specific cation current ( $I_{CAN}$ ) constitute a minimal mechanistic core that produces plateau potentials and bistable firing. Within this framework, the persistent sodium current ( $I_{NaP}$ ) promotes plateau generation, in contrast to the  $Ca^{2+}$ -dependent  $K^+$  current ( $I_{KCa}$ ) which opposes it. These results delineate ionic dependencies at the level of interactions rather than spatial localization and provide a tractable basis for interpreting altered motoneuron excitability in disease.

KEYWORDS

motoneuron, bistability, modeling, plateau potential, spinal cord

## Introduction

Motoneurons show a variety of non-linear intrinsic behaviors that determine their input-output properties (Binder et al., 2020). Among them, bistability allows motoneurons to toggle between two stable states: a quiescent resting state, and a self-sustained firing state characterized by a regular pattern of action potentials generated in absence of synaptic drive. A short excitatory input can trigger a transition from the quiescent state to the active state, whereas a brief inhibitory input can induce the opposite transition (Hultborn et al., 1975; Hounsgaard et al., 1984). The underlying mechanism of the bistability involves formation of plateau potentials, long-lasting membrane depolarizations, during which the motoneuron firing is maintained (Hounsgaard et al., 1988a; Hounsgaard and Mintz, 1988). Persistent firing described in motor units in intact animals (Eken et al., 1989; Eken and Kiehn, 1989; Kiehn and Eken, 1997) as well as in humans

(Gorassini et al., 1998, 1999; Collins et al., 2001) provides indirect evidence that motoneuron bistability is an important feature of motor control contributing to many behaviors. It has been suggested that bistability is involved in postural control lessening the requirement for continuous synaptic drive (Hounsgaard et al., 1988a; Lee and Heckman, 1998a; Heckman et al., 2009). Consistent with this, limiting motoneuron bistability was shown to impair postural control (Bos et al., 2021).

Early studies proposed that bistability primarily resulted from a persistent component of the calcium current  $(I_{Cal.})$  (Hounsgaard and Mintz, 1988; Hounsgaard and Kiehn, 1989) conducted through Cav1.3 channels (Carlin et al., 2000; Simon et al., 2003; Zhang et al., 2006). However, subsequent research has shown that bistability results from a more complex interaction of several ionic currents (Bouhadfane et al., 2013), including the calcium-activated nonspecific cation current (ICAN) through the Transient Receptor Potential Melastatin 5 (TRPM5) channels (Bos et al., 2021) and the persistent sodium current ( $I_{NaP}$ ) via Nav1.6 channels (Drouillas et al., 2023). The emerging picture is a causal sequence of cellular processes: the initial membrane depolarization activates  $I_{NaP}$ , triggering firing and calcium influx; ICaL increases intracellular calcium, which then activates calcium-induced calcium release (CICR) and recruits  $I_{CAN}$ , leading to further depolarizing of the membrane. This cascade of depolarization and triggered currents leads to self-sustained firing, reinforcing the positive feedback loop underlying bistability. The contribution of these intrinsic processes to motoneuron bistability is closely tied to cell size with larger motoneurons exhibiting both higher current expression and a greater propensity for bistable behavior (Harris-Warrick et al., 2024).

Bistability is modulated by neuromodulatory and biophysical contexts. Monoamines released from supraspinal centers can promote and unmask bistability in motoneurons with its latent or partial expression (Conway et al., 1988; Hounsgaard et al., 1988a; Hounsgaard and Kiehn, 1989; Perrier and Delgado-Lezama, 2005). Temperature also modulates bistability: values above 30 °C unmask plateau potentials by recruiting thermosensitive currents mediated by TRPM5 channels (Bos et al., 2021).

Beyond its physiological role, bistability has critical implications in pathology. Following spinal cord injury, excessive bistability in motoneurones has been linked to spasticity, a disabling condition characterized by involuntary muscle contractions (Bennett et al., 2001; Heckman et al., 2008) arising from dysregulated intrinsic ionic currents that amplify self-sustained firing and disrupt motor control (Brocard et al., 2016; Murray et al., 2010).

Despite significant progress, the integration of multiple ionic mechanisms underlying bistability remains poorly understood. Most prior studies often examined individual currents in isolation, such as  $I_{NaP}$ ,  $I_{CaL}$  or  $I_{CAN}$  without considering how their non-linear interactions jointly generate and stabilize bistable firing. In this study, we combine computational modeling, using a conductance-based single-compartment motoneuron model, with mouse spinal slice recordings to dissect how these currents, considered separately and in combination, control the emergence, maintenance and modulation of bistability in motoneurons. Our goal is to identify a minimal mechanistic core of motoneuron bistability at the level of ionic interactions.

# **Methods**

# Modeling methods

## Motoneuron model

We used a conductance-based single-compartment mathematical model of a motoneuron that includes the main spike-generating channels, fast sodium  $(I_{NaF})$  and potassium rectifier  $(I_{Kdr})$ , as well as the persistent sodium  $(I_{NaP})$ , slowly inactivating potassium  $(I_{Kv1.2})$ , high-voltage activated calcium  $(I_{CaL})$ ,  $Ca^{2+}$ -activated, non-specific cation  $(I_{CAN})$ , associated with TRPM5 channels) and  $Ca^{2+}$ -dependent potassium  $(I_{KCa})$ , associated with SK channels) current.

The voltage dynamics are described by the current balance equation:

$$C \cdot \frac{dV}{dt} = -I_{NaF} - I_{NaP} - I_{Kdr} - I_{Kv1.2} - I_{CaL} - I_{KCa} - I_{CAN} - I_{L} + I_{ini}$$
 (1)

where V is membrane potential in mV, t is time in ms, C is membrane capacitance ( $C=1~\mu F\cdot cm^{-2}$ ), and the right hand side of the equation contains all transmembrane currents described as follows.

Fast sodium current (Booth et al., 1997):

$$I_{NaF} = g_{NaF} \cdot m_{NaF}(V)^{3} \cdot h_{NaF} \cdot (V - E_{Na});$$

$$m_{NaF}(V) = (1 + \exp(-(V + 35)/7.8))^{-1};$$

$$\tau_{NaF}(V) \cdot \frac{dh_{NaF}}{dt} = h_{NaF\infty}(V) - h_{NaF};$$

$$\tau_{NaF}(V) = 30 \cdot (\exp((V + 50)/15) + \exp(-(V + 50)/16))^{-1};$$

$$h_{NaF\infty}(V) = (1 + \exp((V + 55)/7))^{-1},$$

$$g_{NaF} = 120 \text{ mS/cm}^{2}, E_{Na} = 55 \text{ mV}.$$

The persistent sodium current was assumed to be non-inactivating. Activation was assumed instantaneous and non-inactivating. Activation dependence on voltage was taken from (Brocard et al., 2013):

$$I_{NaP} = g_{NaP} \cdot m_{NaP}(V) \cdot h_{NaP} \cdot (V - E_{Na});$$
  
 $m_{NaP}(V) = (1 + \exp(-(V + 53)/3))^{-1};$ 

Persistent sodium current is assumed non-inactivating, i.e.  $h_{NaP}=1.$ 

Potassium rectifier current (Booth et al., 1997):

$$I_{Kdr} = g_{Kdr} \cdot m_{Kdr}^{4} \cdot (V - E_{K});$$

$$\tau_{Kdr}(V) \cdot \frac{dm_{Kdr}}{dt} = m_{Kdr\infty}(V) - m_{Kdr};$$

$$\tau_{Kdr}(V) = 7 \cdot (\exp((V + 40)/40) + \exp(-(V + 40)/50))^{-1};$$

$$m_{Kdr\infty}(V) = (1 + \exp(-(V + 28)/15))^{-1};$$

$$g_{Kdr} = 100 \text{ mS/cm}^{2}, E_{K} = 26.54 \cdot \log([K^{+}]_{o}/[K^{+}]_{i}),$$

$$[K^{+}]_{i} = 140 \text{ mM}, [K^{+}]_{o} \in [4, 12] \text{ mM}.$$

Slowly inactivating potassium current (Bos et al., 2018):

$$I_{Kv1.2} = g_{Kv1.2} \cdot m_{Kv1.2} \cdot h_{Kv1.2} \cdot (V - E_K);$$

$$\tau_{Kv1.2}^{x}(V) \cdot \frac{dx_{Kv1.2}}{dt} = x_{Kv1.2\infty}(V) - x_{Kv1.2}, x \in \{m, h\};$$

$$\tau_{Kv1.2}^{m}(V) = 2.44 + 18.387 \cdot (\exp(-(V - 25.645) - (21.633) + \exp((V + 4.42)/45.9))^{-1};$$

$$m_{Kv1.2\infty}(V) = (1 + \exp(-(V + 46)/6.9))^{-1};$$

$$\tau_{Kv1.2}^{h}(V) = 74.74 \cdot (0.00015 \cdot \exp(-(V + 13)/15) + 0.06 \cdot (1 + \exp(-(V + 68)/12))^{-1})^{-1};$$

$$h_{Kv1.2\infty}(V) = (1 + \exp((V + 54)/7.1))^{-1};$$

$$g_{Kv1.2} \in [0, 10] \ mM.$$

High-voltage calcium  $L(I_{CaL})$  current (Jasinski et al., 2013):

$$I_{CaL} = g_{CaL} \cdot m_{CaL} \cdot h_{CaL} \cdot (V - E_{Ca});$$

$$\tau_{CaL}^{x} \cdot \frac{dx_{CaL}}{dt} = x_{CaL\infty}(V) - x_{CaL}, x \in \{m, h\};$$

$$m_{CaL\infty}(V) = (1 + \exp(-(V + 27.5)/5.7))^{-1};$$

$$h_{CaL\infty}(V) = (1 + \exp((V + 52.4)/5.2))^{-1};$$

$$E_{Ca} = 80 \ mV, \ g_{CaL} = 0.05 \ mS/cm^{2}, \ \tau_{CaL}^{m} = 0.5 \ ms,$$

$$\tau_{CaL}^{h} = 18 \ ms.$$

Calcium-activated non-specific cation ( $I_{CAN}$ ) current (Toporikova and Butera, 2011):

$$I_{CAN} = g_{CAN} \cdot \frac{Ca}{Ca + K_{CAN}} \cdot (V - E_{CAN}),$$
 
$$K_{CAN} = 0.74 \cdot 10^{-3} \ mM, \ E_{CAN} = 0 \ mV.$$

Calcium-dependent potassium current ( $I_{KCa}$ ) (Booth et al., 1997). This current was modified to be instantaneous:

$$I_{KCa} = g_{KCa} \cdot \frac{Ca}{Ca + K_d} \cdot (V - E_K), \ K_d = 0.2 \cdot 10^{-3} \ mM.$$

Leak current:

$$I_L = g_L \cdot (V - E_L), g_L = 0.1 \text{ mS/cm}^2, E_L = -80 \text{ mV}.$$

The two currents described above  $(I_{CAN} \text{ and } I_{KCa})$  depend on the intracellular  $Ca^{2+}$  concentration  $[Ca^{2+}]_i$  in mM (denoted by Ca in the equations). The  $Ca^{2+}$  concentration increases directly from the influx of calcium ions through calcium channels (captured by  $I_{CaL}$  in the mathematical model) and indirectly from the release of calcium ions from intracellular stores via a calcium-induced calcium release (CICR) mechanism. Additionally, they are pumped out by the Ca-ATP pumps.

The dynamics of intracellular calcium concentration (*Ca*) in our model are described by the differential equation:

$$\frac{dCa}{dt} = -f \cdot \alpha \cdot I_{CaL} + k_{CICR} \cdot Ca - Ca/\tau_{Ca}.$$
 (2)

On the right hand side of this equation, the first term represents calcium influx through high-threshold, voltage-gated calcium channels ( $I_{CaL}$ ) which open during action potentials. Here f

= 0.01 defines the ratio of entered Ca<sup>2+</sup> ions remaining unbound; the coefficient  $\alpha=(2\cdot F\cdot \delta)^{-1}$  converts inward  $I_{CaL}$  current to  $Ca^{2+}$  concentration rate of change; here F is Faraday's constant ( $F=9.648\cdot 10^4$  C/mol) and  $\delta$  is the thickness (0.1  $\mu$ m) of the shell adjacent to the membrane. Based on these parameters,  $\alpha=5\cdot 10^{-4}~mM\cdot cm^2\cdot ms^{-1}\cdot \mu A^{-1}$ .

The second term describes an increase of cytoplasmic  $Ca^{2+}$  concentration through the CICR mechanism, where the rate of calcium release from internal stores is proportional to the intracellular  $Ca^{2+}$  concentration (defined by  $k_{CICR}$ ). The third term describes the action of calcium pumps (both plasma membrane and SERCA) which rapidly remove calcium from the cytoplasm, with a time constant  $\tau_{Ca} = 10 \ ms$ .

## Qualitative analysis

To investigate the bistable behavior of spinal motoneurons, we implemented a current ramp simulation protocol designed to probe the transitions between quiescent and self-sustained firing states. This approach leverages a linearly varying injected current  $(I_{inj})$  to systematically explore the system's response across a range of input intensities, making it an effective tool for detecting hysteresis and state-dependent dynamics in neuronal models.

The protocol was designed as follows: the injected current was initially set to zero and then increased linearly to a predetermined maximum value (ascending phase) over a specified duration. Subsequently, the current was decreased linearly back to zero (descending phase) at the same rate. This bidirectional ramp allowed us to identify two key transition points: the current threshold at which the system shifts from silence to spiking during the ascending phase  $(I_{up})$  and the lower threshold at which spiking ceases during the descending phase  $(I_{down})$ . Bistability is indicated when  $I_{down}$  is less than  $I_{up}$ , revealing a range of current values where the system can stably maintain either state, depending on its prior condition. This hysteresis reflects the non-linear properties of the model and its history-dependent behavior. To ensure the reliability of these thresholds, the ramp time was progressively increased until the current thresholds for transition to spiking  $(I_{up})$  and for return to silence  $(I_{down})$  stabilized. , confirming that the observed transitions were not influenced by transient dynamics. Ramp durations of several seconds per phase were typically sufficient; longer ramps produced nearly identical  $I_{up}$  and  $I_{down}$  values, confirming that ramp velocity no longer influenced the hysteresis width.

The results of this protocol are presented in injected current-voltage (I–V) bifurcation diagrams. These diagrams depict the steady-state voltage response as a function of the injected current, delineating the regions corresponding to quiescence, repetitive spiking, and bistability. The upward and downward branches correspond to the ascending and descending phases of the current ramp, respectively, thereby illustrating the distinct transition thresholds ( $I_{up}$  and  $I_{down}$ ) and the hysteresis loop between them. For interpretation, the I–V bifurcation diagram provides a compact representation of how the system's qualitative behavior changes with input strength, serving as a graphical summary of the underlying non-linear dynamics and the coexistence of multiple stable states.

Equilibrium points of our single-compartment model, which represent the steady-state solutions of the system, were incorporated into the bifurcation diagrams. These points were determined by setting the net membrane current (the right-hand side of Equation 1) to zero. For each fixed value of injected current ( $I_{inj}$ ), the gating variables and intracellular calcium concentration were assigned their steady-state values. The corresponding equilibrium membrane potential was then numerically obtained by solving the aforementioned equation for V. By collecting these steady-state points across a range of  $I_{inj}$ , one or more branches of the equilibrium voltage were formed.

To further validate the protocol's ability to detect bistability, we employed a complementary current step simulation inspired by experimental approaches. Starting from a baseline of  $I_{inj} = 0$ , the current was stepped to an intermediate value within the suspected bistable range  $(I_{down} < I_{inj} < I_{up})$ , then increased to a level above  $I_{up}$ , and subsequently returned to the intermediate value before returning to zero. This sequence demonstrated that, at the intermediate current level, the system's state, silent or spiking, depended on its prior activation history, reinforcing the findings of the ramp protocol.

The current ramp simulations also supported parametric analyses by varying key model parameters and plotting the resulting bifurcation diagrams. These diagrams mapped the system's equilibrium points and oscillatory regimes as functions of  $I_{inj}$ , providing a visual representation of the bistable region. The protocol's design, with its carefully adjusted ramp duration, ensured that the gradual variation of input current effectively captured the boundaries of this region, offering a robust technical framework for studying the conditions under which bistability emerges and persists in the model.

# Simulations

Simulations were performed using custom-written C++ and Julia software. Integration was performed by the Dormand-Prince 5(4) method using (Boost Development Team, n.d.). Source code written in C++ and Julia for the model and examples of the ramping protocols can be found in the Github repository associated with this manuscript (Jeter and Molkov, 2025).

## **Experimental methods**

## Experimental model

Mice (C57/Bl6 background) were housed under a 12h light/dark cycle with *ad libitum* access to water and food. Room temperature was kept between 21 and 24 °C and between 40 and 60% relative humidity. All animal care and use were conformed to the French regulations (Décret 2010-118) and approved by the local ethics committee (Comité d'Ethique en Neurosciences INT-Marseille, CE71 Nb A1301404, authorization Nb #50133-2024060612594852).

# *In vitro* preparations

For the slice preparation, mice were cryoanaesthetized (P5-P7) or anesthetized (P8-P11) with intraperitoneal injection of a mixture

of ketamine/xylazine (100 and 10 mg/kg, respectively). They were then decapitated, eviscerated and the spinal cord removed by laminectomy, and placed in a Sylgard-lined petri dish with ice-cold (+4 °C) artificial CSF (aCSF) solution composed of the following (in mM): 252 sucrose, 3 KCl, 1.25 KH<sub>2</sub>PO<sub>4</sub>, 4 MgSO<sub>4</sub>, 0.2 CaCl<sub>2</sub>, 26 NaHCO<sub>3</sub>, 25 D-glucose, pH 7.4. The meninges were removed and the lumbar spinal cord was then introduced into a 1% agar solution, quickly cooled, mounted in a vibrating microtome (Leica, VT1000S) and sliced (325  $\mu$ m) through the L4–5 lumbar segments. Slices were immediately transferred into the holding chamber filled with bubbled (95% O<sub>2</sub> and 5% CO<sub>2</sub>) aCSF solution composed of (in mM): 120 NaCl, 3 KCl, 1.25 NaH<sub>2</sub>PO<sub>4</sub>, 1.3 MgSO<sub>4</sub>, 1.2 CaCl<sub>2</sub>, 25 NaHCO<sub>3</sub>, 20 D-glucose, pH 7.4, 30–32 °C. After a 30–60 min resting period, individual slices were transferred to a recording chamber continuously perfused with aCSF heated to 32–34 °C.

## In vitro recordings

Whole-cell patch-clamp recordings were performed using a Multiclamp 700B amplifier (Molecular Devices) from L4-L5 motoneurons with the largest soma (>400 μm<sup>2</sup>) located in the lateral ventral horn. These cells are the most likely to correspond to large, fast-type motoneurons, which are those most prone to expressing bistable behavior and plateau potentials (Harris-Warrick et al., 2024). A total of 17 motoneurons that met the inclusion criteria described below were successfully recorded from 12 neonatal mice. Motoneurons were isolated from most rapid synaptic inputs with a combination of kynurenic acid (1.5 mM), picrotoxin (100  $\mu$ M) and strychnine (1  $\mu$ M) to block glutamatergic, fast GABAergic and glycinergic synapses, respectively. Patch electrodes (2–4 M $\Omega$ ) were pulled from borosilicate glass capillaries (1.5 mm OD, 1.12 mm ID; World Precision Instruments) on a Sutter P-97 puller (Sutter Instruments Company) and filled with an intracellular solution (in mM): 140 K+-gluconate, 5 NaCl, 2 MgCl<sub>2</sub>, 10 HEPES, 0.5 EGTA, 2 ATP, 0.4 GTP, pH 7.3. Pipette and neuronal capacitive currents were canceled and, after breakthrough, the series resistance was compensated and monitored. Recordings were digitized on-line and filtered at 20 kHz through a Digidata 1550B interface using Clampex 10.7 software (Molecular Devices). All experiments were designed to gather data within a stable period (i.e., at least 2 min after establishing whole-cell access).

## Drug list

All solutions were oxygenated with 95%  $O_2/5\%$   $CO_2.$  All salt compounds, as well as veratridine (40 nM), apamin (200 nM), kynurenate (1.5 mM), picrotoxin (100  $\mu$ M), strychnine (1  $\mu$ M) were obtained from Sigma-Aldrich.

# Data quantification

Electrophysiological data analyses were analyzed off-line with Clampfit 10.7 software (Molecular Devices). For intracellular recordings, several basic criteria were set to ensure optimum quality of intracellular recordings. Only cells exhibiting a stable resting membrane potential, access resistance ( $\leq\!20~\mathrm{M}\Omega$  with no > 20% variation) and an action potential amplitude (measured from threshold to peak) larger than 40 mV under normal aCSF were

considered. Passive membrane properties of cells were measured by determining from the holding potential the largest voltage deflections induced by small current pulses that avoided activation of voltage-sensitive currents. We determined input resistance by the slope of linear fits to voltage responses evoked by small positive and negative current injections. The peak amplitude of the slow afterdepolarization (slow ADP or sADP) was defined as the difference between the holding potential and the peak voltage deflection after the burst of spikes. The sADP area was measured between the end of the stimulus pulse and the onset of the hyperpolarizing pulse (delta= 7.5 s). If necessary, using bias currents, the pre-pulse membrane potential was maintained at the holding potential fixed in the control condition. Bistable properties were investigated using a 2 s depolarizing current pulses of varying amplitudes (0.8-2 nA). To assess the ability of a motoneuron to express bistability, the holding current was gradually increased in 25 pA increments thereby shifting the membrane potential (Vh) toward more depolarized values before delivering the depolarizing current pulse. This protocol, previously described and illustrated in detail in our earlier work [e.g., Supplementary Figure 1C in Bos et al. (2021)], was repeated until the neuron reached its spiking threshold. A cell was considered as bistable when (1) the prestimulus membrane potential remained hyperpolarized below the spiking threshold (downstate), (2) the post-stimulus membrane potential remained depolarized above the spike threshold (upstate), and (3) the membrane potential could return to downstate after a brief hyperpolarizing pulse. To quantify the extent of bistability, we measured both the voltage (V) range between the most hyperpolarized holding potential (Vh min, from which a plateau could still be induced) and the most depolarized holding potential (Vh max, at which the plateau could be maintained), and the corresponding range of injected currents ( $\Delta I$ ) over which bistable behavior was observed.

## **Statistics**

When two conditions (control vs. drugs) were compared, we used the Wilcoxon matched pairs test. For all statistical analyses, the data met the assumptions of the test and the variance between the statistically compared groups was similar. The level of significance was set at p < 0.05. Statistical analyses were performed using Graphpad Prism 7 software.

# Results

# Calcium dynamics and calcium-dependent currents

# The role of calcium-induced calcium release (CICR) mechanism

A brief excitatory current pulse into a motoneuron triggers a train of action potentials, causing a substantial increase in intracellular calcium levels ( $[Ca^{2+}]_i$ ). This increase is driven by influx via voltage-gated calcium channels, further amplified by calcium-induced calcium release (CICR) from internal stores. The resulting  $[Ca^{2+}]_i$  accumulation activates two  $Ca^{2+}$ -dependent currents with opposing effects: the depolarizing calcium-activated

non-specific cation current ( $I_{CAN}$ ) and the hyperpolarizing calcium-dependent potassium current ( $I_{KCa}$ ).

We first tested the hypothesis that CICR is essential for amplifying intracellular calcium to levels sufficient for activating calcium-dependent currents underlying bistability, a key step in the ionic cascade proposed in the Introduction. We modeled  $[Ca^{2+}]_i$  dynamics and compared scenarios with and without CICR.As described in Methods, the  $[Ca^{2+}]_i$  dynamics in our model are governed by the differential (Equation 2). The calcium clearance pump operates with a time constant of  $\tau_{Ca}=10$  ms, which, in the absence of CICR, would clear all calcium introduced by a spike before the next spike. The term  $k_{CICR} \cdot Ca$  in Equation 2 captures the CICR mechanism, where the rate of calcium release from internal stores is directly proportional to the current calcium concentration Ca with coefficient  $k_{CICR}$ .

For simplicity, the intracellular calcium dynamics described by Equation 2 can be expressed as:

$$\frac{dCa}{dt} = -f \cdot \alpha \cdot I_{CaL} - Ca/\tau_{eff},$$

where  $au_{eff}$  represents the effective time constant

$$\tau_{eff} = (1/\tau_{Ca} - k_{CICR})^{-1}$$
.

The gain  $k_{CICR}$  must not exceed  $1/\tau_{Ca}$  to prevent negative  $\tau_{eff}$ , which would lead to an infinite increase in calcium. In our model,  $k_{CICR}$  is set at  $0.096~{\rm ms}^{-1}$ , yielding an effective time constant  $\tau_{eff}=250~{\rm ms}$ . This value was chosen phenomenologically to match typical slow afterdepolarization decay rates observed in our *in vitro* data and prior studies.

This prolonged  $\tau_{e\!f\!f}$  (compared to  $\tau_{Ca}$ ) reflects how the CICR mechanism substantially slows calcium clearance, resulting in  $[\mathrm{Ca}^{2+}]_i$  build-up during repetitive firing. As shown in Figure 1, calcium levels sharply increase in response to a rectangular current pulse, strongly activating  $I_{CAN}$  and  $I_{KCa}$ . Without CICR ( $k_{CICR}=0$ ), pumps clear calcium rapidly between spikes, preventing significant accumulation during repetitive firing. Consequently, in the absence of sustained elevations in intracellular  $Ca^{2+}$ , neither  $I_{CAN}$  nor  $I_{KCa}$  currents are activated to a significant degree.

These analyses support our hypothesis, demonstrating that CICR slows calcium clearance and is necessary for the sustained  $[Ca^{2+}]_i$  elevation.

# Interplay between $I_{CAN}$ and $I_{KCa}$ : afterdepolarization vs. afterhyperpolarization

Intracellular recordings have shown that motoneurons demonstrate two post-stimulus behaviors: a slow afterdepolarization (sADP) after brief excitatory inputs, typical for a bistable motoneuron type, and an afterhyperpolarization (AHP) observed in a non-bistable motoneuron type (Harris-Warrick et al., 2024). We hypothesized that the balance between  $I_{CAN}$  and  $I_{KCa}$  determines post-stimulus behavior and bistability, with  $I_{CAN}$  dominance favoring sADP and bistability, while  $I_{KCa}$  dominance promotes AHP, aligning with observed differences in motoneuron subtypes. To test this, we simulated responses to depolarizing current pulses, varying the relative strengths of these currents.

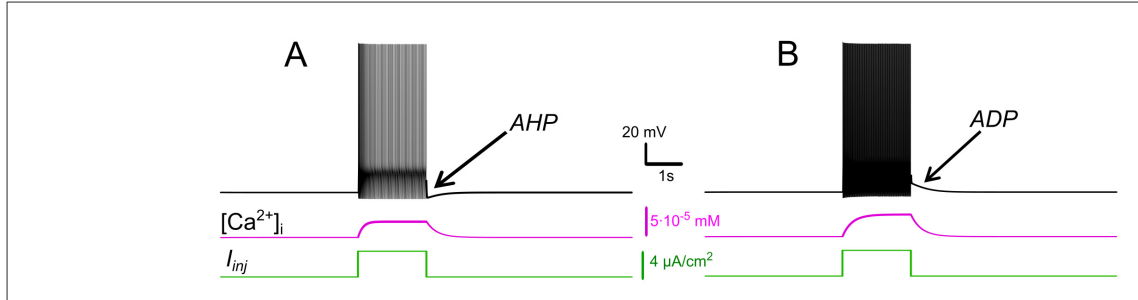


FIGURE 1

Effects of  $I_{KCa}$  vs. effects of  $I_{CAN}$ . Membrane potential (black) and intracellular  $Ca^{2+}$  (magenta) in response to step current (green). Intracellular  $Ca^{2+}$  concentration increases during spiking activity and then slowly adapts. (A) When  $I_{KCa}$  is stronger than  $I_{CAN}(g_{KCa}=0.5\,\text{mS},\,g_{CAN}=0.7\,\text{mS})$ , this leads to after-depolarization (AHP). (B) When  $I_{CAN}$  is stronger than  $I_{KCa}$  ( $g_{KCa}=0.5\,\text{mS},\,g_{CAN}=0.7\,\text{mS}$ ), this leads to after-depolarization (ADP) immediately following spiking activity.

Our simulations show that when  $I_{KCa}$  predominates,  $Ca^{2+}$ -dependent potassium efflux produces hyperpolarization of the membrane and a decrease in excitability. This effect promotes a prominent post-stimulus AHP supported by sustained  $[Ca^{2+}]_i$  elevation (Figure 1A). Conversely, when  $I_{CAN}$  predominates, the elevation of  $[Ca^{2+}]_i$  activates this current, leading to a depolarizing influx of sodium, that in turn increases the firing frequency during the pulse and yields an sADP afterward (Figure 1B). As  $[Ca^{2+}]_i$  declines, the membrane potential slowly relaxes back toward its resting values.

The sADP may be directly linked to neuronal bistability because it provides a sustained depolarizing drive that maintains the neuron in a high-activity state through positive feedback. Therefore, these model behaviors support our hypothesis and provide a mechanistic interpretation:  $I_{CAN}$  biases toward sADP and plateau maintenance, whereas  $I_{KCa}$  biases toward AHP and termination of spiking.

# Mechanisms of I<sub>CAN</sub>-based bistability and their modulation

## I<sub>CAN</sub>-based bistability

We then hypothesized that  $I_{CAN}$  provides a robust mechanism for bistability via a positive feedback loop sustaining depolarization post-stimulus. We tested this using ramp and step current protocols in the model, analyzing bifurcation diagrams as  $g_{CAN}$  varied. Ramp and step protocols were chosen because they are the standard experimental approaches used to investigate motoneuron bistability: ramps reveal firing hysteresis, whereas steps assess plateau potentials and self-sustained firing (Hounsgaard and Kiehn, 1985; Hounsgaard and Mintz, 1988; Hounsgaard et al., 1988a; Lee and Heckman, 1998b,a; Li and Bennett, 2003).

Our model simulations support that the expression of  $I_{CAN}$  provides a robust route to bistability. The process begins with the opening of voltage-gated calcium channels during each action potential. While this influx alone is insufficient to fully activate  $I_{CAN}$ , it triggers CICR, which amplifies  $[Ca^{2+}]_i$  (see below).

The elevated  $[Ca^{2+}]_i$  activates  $I_{CAN}$  establishing a positive feedback loop:  $I_{CAN}$  sustains depolarization, promoting continuous firing; spikes further elevate  $[Ca^{2+}]_i$  via  $Ca^{2+}$  entry and CICR, and thus reinforce  $I_{CAN}$  activation. This self-perpetuating mechanism

allows the motoneuron to remain in a high-activity state (persistent spiking) even after the initial stimulus is removed, creating bistability: the neuron can operate in either a quiescent state or an active spiking state.

The 2-parameter bifurcation diagram (Figure 2A) shows how  $I_{CAN}$  controls the appearance and the extent of the bistability region. For each  $g_{CAN}$ , we replicated the experimental ramp current protocol in the model as described in Methods. To identify bistability, we used a triangular current ramp, consisting of two phases, ascending ("up") and descending ("down"). These correspond to the increasing and decreasing portions of the injected current, respectively. No bistability is seen at  $g_{CAN}$  = 0 (Figures 2A, B). It is appearing when  $g_{CAN}$  starts increasing  $(g_{CAN} > 0$ , Figures 2A, C). Particularly, at  $g_{CAN} = 0.5 \text{ mS/cm}^2$ , the voltage-current relation during a linear Iini ramp (Figure 2C) reveals distinct up  $(I_{up})$  and down  $(I_{down})$  thresholds. At  $g_{CAN}$ = 0,  $I_{down}$  and  $I_{up}$  coincide (no hysteresis; Figure 2B). Once  $g_{CAN}$ becomes large enough, the interval ( $I_{down} < I_{inj} < I_{up}$ ) opens and bistability emerges. This is evident as the current required to trigger spiking during the ramp-up exceeds the current at which spiking stops during ramp-down (Figure 2C). This hysteresis widens with further increases in  $g_{CAN}$  (Figure 2A), reflecting the strengthening of the I<sub>CAN</sub>-mediated positive feedback loop, which supports the self-sustained spiking state.

In Figures 2B, C blue and red traces correspond to ascending and descending phases of the current ramp, respectively. For  $I_{inj} < I_{up} = 1.7 \, \mu \text{A/cm}^2$ , the system displays two attracting regimes separated by an unstable equilibrium (saddle): a stable hyperpolarized state corresponding to the resting state (silent) and a stable spiking state (limit cycle) (Figure 2C). As  $I_{inj}$  exceeds  $I_{up} = 1.7 \, \mu \text{A/cm}^2$ , the low potential stable branch of the V-nullcline merges with the saddle and vanishes via a fold bifurcation, and the system transitions to a stable limit cycle representing a repetitive spiking regime. During the descending phase of the ramp, spiking persists until  $I_{inj}$  decreases to  $I_{down} = 1.1 \, \mu \text{A/cm}^2$ , which is less than  $I_{up}$  (Figures 2C, D), yielding a hysteresis interval ( $\Delta I > 0$  with  $I_{down} < I_{up}$ ), indicative of bistability.

To further probe bistability, we implemented a step protocol inspired by experimental methods (Figure 2E). Starting at  $I_{inj}=0$  in a silent state, we applied an intermediate pulse within the bistable range  $(I_{down} < I_{inj} < I_{up})$ , then increased it above  $I_{up}$  to induce firing, before returning to the intermediate current (Figure 2E).

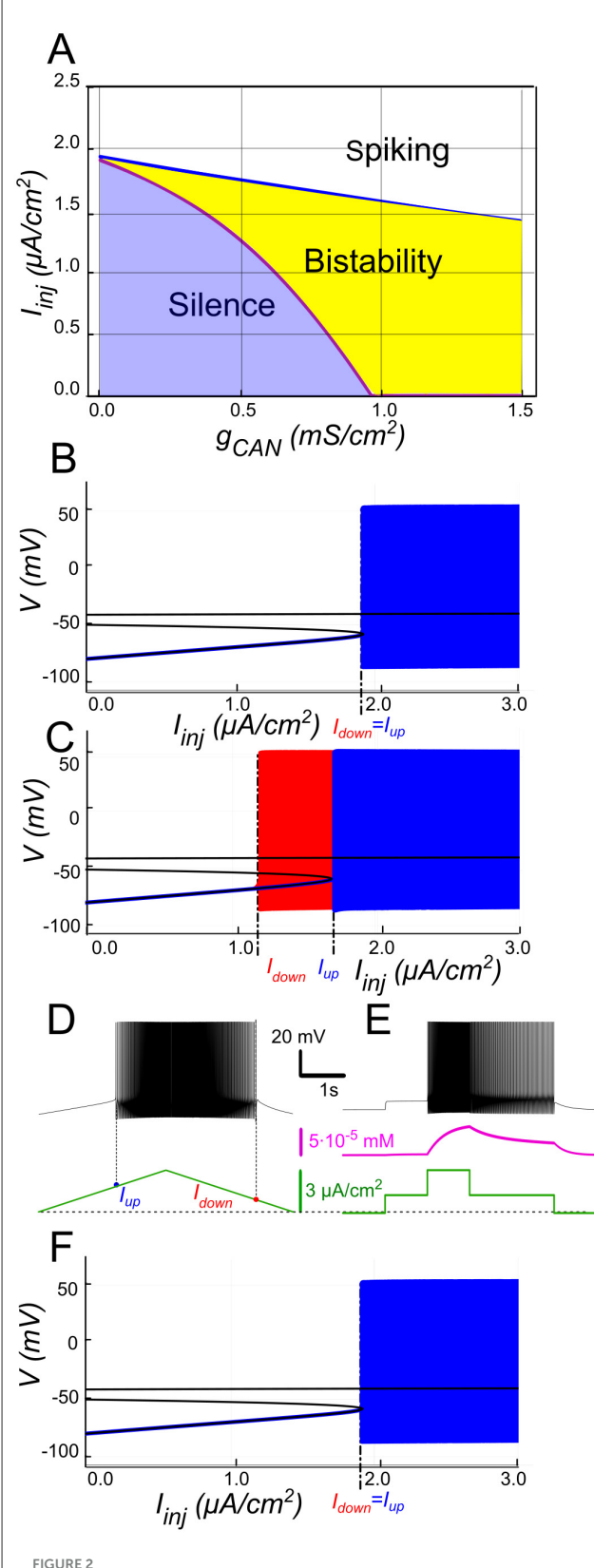


FIGURE 2  $I_{CAN}$ -induced bistability and its disappearance after CICR blockade (A) Parameter plane  $(g_{CAN}, I_{inj})$  partitioned into regions of different

(A) Parameter plane  $(g_{CAN}, l_{inj})$  partitioned into regions of different behaviors  $(g_{KCa} = g_{NaP} = 0)$ . The upper and lower boundaries of the bistability region represent the dependence of  $l_{up}$  (blue line) and  $l_{down}$  (red line) on  $g_{CAN}$ , respectively. With no  $l_{CAN}$  ( $g_{CAN} = 0$ ) the transitions from silence to spiking and back occur at the same

(Continued)

#### FIGURE 2 (Continued)

 $I_{ini}$  values signifying no bistability. As  $g_{CAN}$  increases,  $I_{down}$  becomes smaller than  $I_{up}$ , with the bistability range progressively expanding. (B, C) Bifurcation diagrams showing different behaviors of the system at  $g_{CAN} = 0$  and  $g_{CAN} = 0.5$  mS/cm<sup>2</sup> across a range of the injected current values,  $I_{inj}$ . Black lines depict the system's unstable equilibrium states. Blue traces represent silence or spiking during the ascending current ramp; red traces indicate firing during the descending current ramp (when different from the ascending ramp). When  $I_{inj} < I_{up}$  there is a stable hyperpolarized state (stable node). If  $I_{inj}$  is increased over  $I_{up}$ , the system transitions to spiking, covering the voltage range shown in red and blue. This stable spiking regime exists in the range  $I_{ini} > I_{down}$ . When  $I_{ini}$  is reduced below  $I_{down}$ , the limit cycle representing spiking disappears, and the system transitions to the low voltage stable fixed point. Between these bifurcation points the hyperpolarized state (silence) coexists with the stable limit cycle (spiking) shown in red. (D, E) Bistability revealed with ramp and step protocols. (D) Iini was linearly increased from 0 to 3  $\mu$ A/cm<sup>2</sup> and back (green). Note that spiking started at higher current than the transition back to silence ( $I_{up} > I_{down}$ ). (E)  $I_{inj}$  was held piecewise constant at 0 first, then increased to 1.5  $\mu A/cm^2$ then to 3, then reduced back to 1.5, and, finally, to 0 (see the black trace at the bottom). At  $I_{inj}=1.5~\mu\text{A/cm}^2$  the system exhibits spiking or silence depending on whether it was active or not during the previous stage. Note the difference in the intracellular calcium concentration levels (green trace). (F) Same representation as in C but with intracellular calcium release blocked ( $k_{CICR} = 0$ ). Note lack of bistability

This protocol showed that, at the same intermediate current value, the motoneuron could either continue firing or remain silent, depending on whether it was previously activated.

The above computational findings support our hypothesis, identifying  $I_{CAN}$  as a key determinant of the bistable behavior through self-sustained spiking.

### The role of CICR

We further hypothesized that CICR is required to raise  $[Ca^{2+}]_i$  enough for  $I_{CAN}$  activation and bistability, as transient influx through voltage-gated calcium channels alone is insufficient. To test this, we set  $k_{CICR}=0$  and repeated ramp protocols. As shown in Figure 2F, when CICR is blocked the  $I_{CAN}$ -based bistability collapses (ramp hysteresis vanishes) because the transient rise in  $[Ca^{2+}]_i$  during spiking activity is almost completely abolished (not shown), as  $Ca^{2+}$  influx through voltage-gated channels alone is rapidly cleared by pumps. Consequently,  $I_{CAN}$  is not recruited, and the system behaves equivalently to simulations where  $g_{CAN}$  is set to zero (Figure 2B). In other words, CICR effectively slows  $Ca^{2+}$  clearance ( $\tau_{eff}$  in the hundreds of ms) and is necessary in this framework to maintain the  $Ca^{2+}$ -dependent depolarizing drive provided by  $I_{CAN}$ . This supports our hypothesis, emphasizing the role of CICR in maintaining the  $I_{CAN}$ -driven feedback loop.

# The role of $I_{KCa}$ in modulating $I_{CAN}$ -based bistability

Hypothesizing that  $I_{KCa}$  opposes  $I_{CAN}$ -based bistability by hyperpolarizing the membrane, we analyzed the model's bifurcation maps varying  $g_{KCa}$  and  $g_{CAN}$ , and validated model predictions with apamin experiments in slices.

Our model supports that  $I_{KCa}$  has a negative effect on  $I_{CAN}$ -based bistability. As  $[Ca^{2+}]_i$  increases, SK-type K<sup>+</sup> channels (mediating  $I_{KCa}$ ) open, allowing intracellular K<sup>+</sup> ions to exit the cell. This outward current hyperpolarizes the membrane, decreasing excitability, and preventing the selfsustaining depolarization provided by ICAN. Bifurcation analyses (Figure 3) summarize this interplay. At low gCAN, a regime where  $I_{KCa}$ dominates the Ca<sup>2+</sup>-dependent response, the neuron transitions between spiking and silence at the same current threshold during ascending and descending current ramps, with this common threshold only weakly influenced by gCAN (Figure 3A). Increasing  $g_{CAN}$  lowers the spiking onset threshold and, once  $g_{CAN}$  reaches approximately 1 mS/cm<sup>2</sup> (Figure 3A), a hysteresis interval opens ( $\Delta I > 0$  when  $I_{down} < I_{up}$ ), indicating the emerging bistability. This is evident as the current required to trigger spiking during the ramp-up exceeds the current at which spiking stops during ramp-down, with the current range  $\Delta I$ supporting bistability, progressively expanding as g<sub>CAN</sub> increases further. Additionally, the specific  $g_{CAN}$  value at which this bifurcation occurs depends linearly on  $g_{KCa}$  (Figure 3B), suggesting that the bistability arises when  $I_{CAN}$  begins to dominate over  $I_{KCa}$ . Equivalently, reducing  $g_{KCa}$  at fixed  $g_{CAN}$  unmasks bistability (Figures 3C-F).

We tested these predictions by performing patch-clamp recordings of lumbar motoneurons, focusing on the effects of apamin (200 nM), a selective blocker of  $I_{KCa}$ . We measured the parameters of the sADP induced by a brief depolarization of the motoneurons. Application of apamin significantly increased the amplitude and area of the sADP, indicating a larger depolarizing response when  $I_{KCa}$  is reduced (Figures 4A–C). In addition, apamin also enhanced the capacity of motoneurons for bistable behavior. Specifically, motoneurons were able to express plateau potentials from more hyperpolarized holding potentials (Figure 4D), reflected by a significant shift in Vhmin (defined as the most negative holding potential from which a plateau could be induced) from  $-59.7\,\mathrm{mV}$  (+/- 5.4) mV to  $-61.9 \ (+/-5.2) \ \text{mV} \ (p < 0.05)$ , accompanied by increases in the voltage range ( $\Delta V = Vh_{max} - Vh_{min}$ , where  $Vh_{max}$  is the most depolarized holding potential at which a plateau could be maintained before reaching action potential threshold) from 4.9 (+/-3.3) mV to 8.2 (+/-1.5) mV (p < 0.05; Figure 4E) and the current range ( $\Delta I$ ) over which bistability was observed from 76.3 (+/-25.9) pA to 109.6 (+/-46.4) pA (p < 0.05; Figure 4F). Together, these results support the prediction of the model that reducing  $I_{KCa}$  expands the bistable regime by reducing the afterhyperpolarizing influence opposing I<sub>CAN</sub>-driven depolarization (Figures 1, 3). These results support our hypothesis, underscoring the antagonistic interplay between  $I_{CAN}$  and  $I_{KCa}$  in shaping motoneuron excitability and providing a mechanistic basis for bistable behaviors.

# Modulation of I<sub>CAN</sub>-based bistability by extracellular potassium concentration

Because  $I_{KCa}$  depends on the  $K^+$  driving force, we hypothesized that elevated  $[K^+]_o$  enhances bistability by depolarizing the potassium reversal potential  $E_K$  and reducing  $I_{KCa}$ 's opposition

to  $I_{CAN}$ .  $E_K$  is set by the Nernst equation which provides the potassium ion equilibrium potential based on the ratio of intracellular  $[K^+]_i$  to extracellular  $[K^+]_o$  potassium concentration (see Methods). Increasing extracellular potassium  $[K^+]_o$  depolarizes  $E_K$  thereby reducing the outward driving force through  $I_{KCa}$ . This weakens the hyperpolarizing influence of  $I_{KCa}$  that counteracts the  $I_{CAN}$ -mediated depolarizing feedback.

We explored this interaction by varying  $[K^+]_o$  and  $g_{CAN}$  in the model while holding  $g_{KCa}$  at 0.5 mS/cm². The resulting two-parameter map (Figure 5B) shows the bistable range (color-coded width  $\Delta I = I_{up} - I_{down}$ , black indicating no bistability) as a function of  $g_{CAN}$  and  $[K^+]_o$ . At low  $[K^+]_o$  (e.g., physiologically normal levels of 4 mM),  $E_K$  is strongly negative and  $I_{KCa}$  efficiently counteracts  $I_{CAN}$ , so relatively large  $g_{CAN}$  (e.g.,  $\sim 1$  mS/cm², Figure 3A) is required for bistability. As  $[K^+]_o$  increases,  $E_K$  depolarizes, weakening  $I_{KCa}$  and the bistable interval opens at progressively lower  $g_{CAN}$  (Figure 5A). For instance, at  $g_{CAN} = 0.9$  mS/cm² the model is not bistable at  $[K^+]_o = 4$  mM (Figure 5C), but becomes bistable at  $[K^+]_o = 8$  mM (Figures 5D, E), with the hysteresis width further expanding as  $[K^+]_o$  rises (Figure 5B). As elsewhere, we corroborated bistable firing behavior using a step protocol showing different coexisting stable regimes at identical inputs (Figure 5F).

Our findings support the hypothesis, suggesting relevance to physiological  $[K^+]_0$  fluctuations: during sustained activity or in certain pathological conditions, elevation of  $[K^+]_0$  can occur, which, by decreasing the effectiveness of  $I_{KCa}$ , would favor expression of the  $I_{CAN}$ -driven positive feedback and broaden the bistable operating range. More generally, these findings illustrate how intrinsic mechanisms of excitability can be tuned by extracellular milieu, here via the dependence of  $E_K$  on  $[K^+]_0$ .

# The role of $I_{NaP}$ in modulating $I_{CAN}$ -based bistability

The persistent sodium current ( $I_{NaP}$ ) is well-known for amplifying neuronal excitability by providing a sustained depolarizing drive at subthreshold voltages (Crill, 1996). Hypothesizing  $I_{NaP}$  facilitates  $I_{CAN}$ -based bistability, we examined its interactions with  $I_{CAN}$  using our computational model (Figure 6). The two-parameter bifurcation map in Figure 6B depicts the bistability range (color-coded as the hysteresis width  $\Delta I = I_{up} - I_{down}$ ) as a function of  $g_{NaP}$  and  $g_{CAN}$ . Overall, the bistable interval expands with increasing  $g_{NaP}$ , indicating that  $I_{NaP}$  enhances the robustness of bistability. For instance, at moderately low  $g_{CAN}$  values (e.g., 0.9 mS/cm²; Figure 6B), where  $I_{CAN}$  alone fails to produce bistability (Figure 6C), elevating  $g_{NaP}$  from zero to 0.45 mS/cm² uncovers a clear hysteresis interval (Figures 6B, D–F), enabling the coexistence of silent and spiking states over a range of injected currents.

This effect aligns with the core  $I_{CAN}$ -driven positive feedback loop underpinning bistability: (i) spiking activity opens voltage-gated calcium channels, leading to  $Ca^{2+}$  influx; (ii) this influx triggers CICR, amplifying the cytosolic  $Ca^{2+}$  signal; (iii) elevated  $[Ca^{2+}]_i$  then activates  $I_{CAN}$ , and (iv) the resulting depolarisation accelerates spiking promoting additional  $Ca^{2+}$  entry and closing the self-reinforcing loop. Amplifying any element of this loop can elevate its overall gain, tipping the system toward bistability.

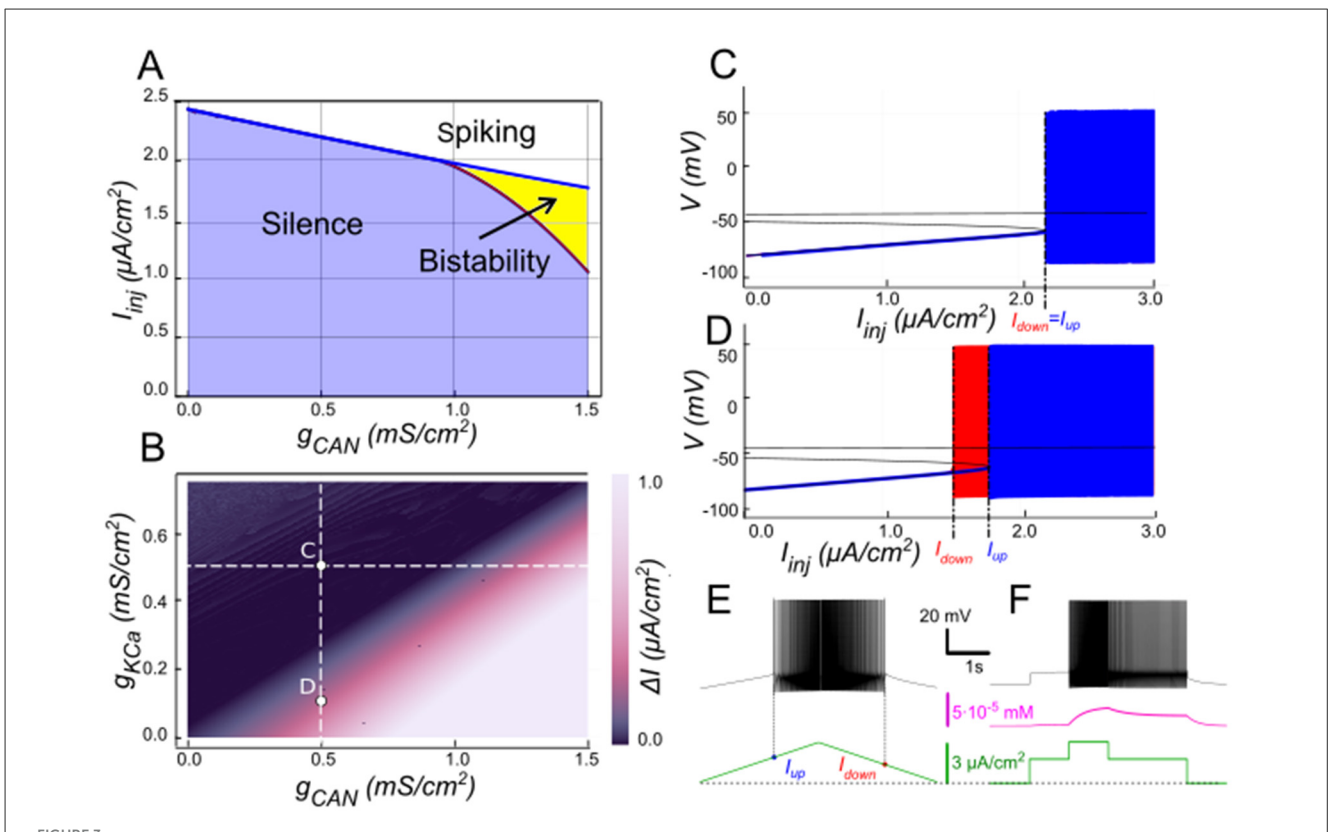


FIGURE 3
Modulation of  $I_{CAN}$ -dependent bistability by  $I_{KCa}$ . (A) Bifurcation diagram similar to Figure 2A, constructed for  $g_{KCa} = 0.5 \text{ mS/cm}^2$ . Note, that unlike in Figure 2, bistability emerges once  $g_{CAN}$  exceeds 1 mS/cm². (B) Bistability range  $\Delta I_{inj}$  depending on  $g_{CAN}$  and  $g_{KCa}$  conductances. Bistability range (defined as  $I_{up} - I_{down}$ ) is color coded. Bistability exists in the lower right part of the diagram. Note near linear dependence of  $g_{CAN}$  bistability threshold on  $g_{KCa}$ . White dashed line shows the value of  $g_{KCa}$  used to construct the bifurcation diagram in (A). (C, D) Bifurcation diagrams showing possible behaviors of the system at the parameter values labeled correspondingly in (B). (C) At higher  $g_{KCa}$  value ( $g_{KCa} = 0.5$ ) transitions from quiescence to spiking and back occur at the same injected current value ( $I_{up} = I_{down}$ ), indicating no bistability. (D) When  $g_{KCa}$  is lowered to 0.1, the transition from spiking to quiescence occurs at a lower injected current than the transition from quiescence to spiking ( $I_{down} < I_{up}$ ), so spiking shown in red coexists with the silent regime. (C, D) Blue indicates activity during the ascending current ramp and red indicates activity during the descending current ramp. (E, F) Ramp (left) and step (right) current injection protocols, illustrating bistability revealed in (D). The intermediate current step is between  $I_{down}$  and  $I_{up}$ . The system's state depends on whether it was active or not at the previous step, exhibiting bistable behavior.

Here,  $I_{NaP}$  contributes by delivering a tonic depolarizing current that lowers the voltage threshold for spike initiation and Ca<sup>2+</sup> entry. This facilitates the recruitment of  $I_{CAN}$  during the onset of activity and bolsters its ability to sustain the high-activity state once engaged, even at lower  $g_{CAN}$  levels. For example, at  $g_{CAN} = 0.9 \text{ mS/cm}^2$  and  $g_{NaP} = 0.45 \text{ mS/cm}^2$ , the model displays robust bistability (Figures 6D–F), whereas reducing  $g_{NaP}$  to 0 eliminates it (Figure 6C). However, at lower  $I_{CAN}$  expression (e.g., at  $g_{CAN} = 0.5 \text{ mS/cm}^2$ ),  $I_{NaP}$ -evoked depolarization is insufficient to achieve the high-gain regime needed for bistability at any  $g_{NaP}$ .

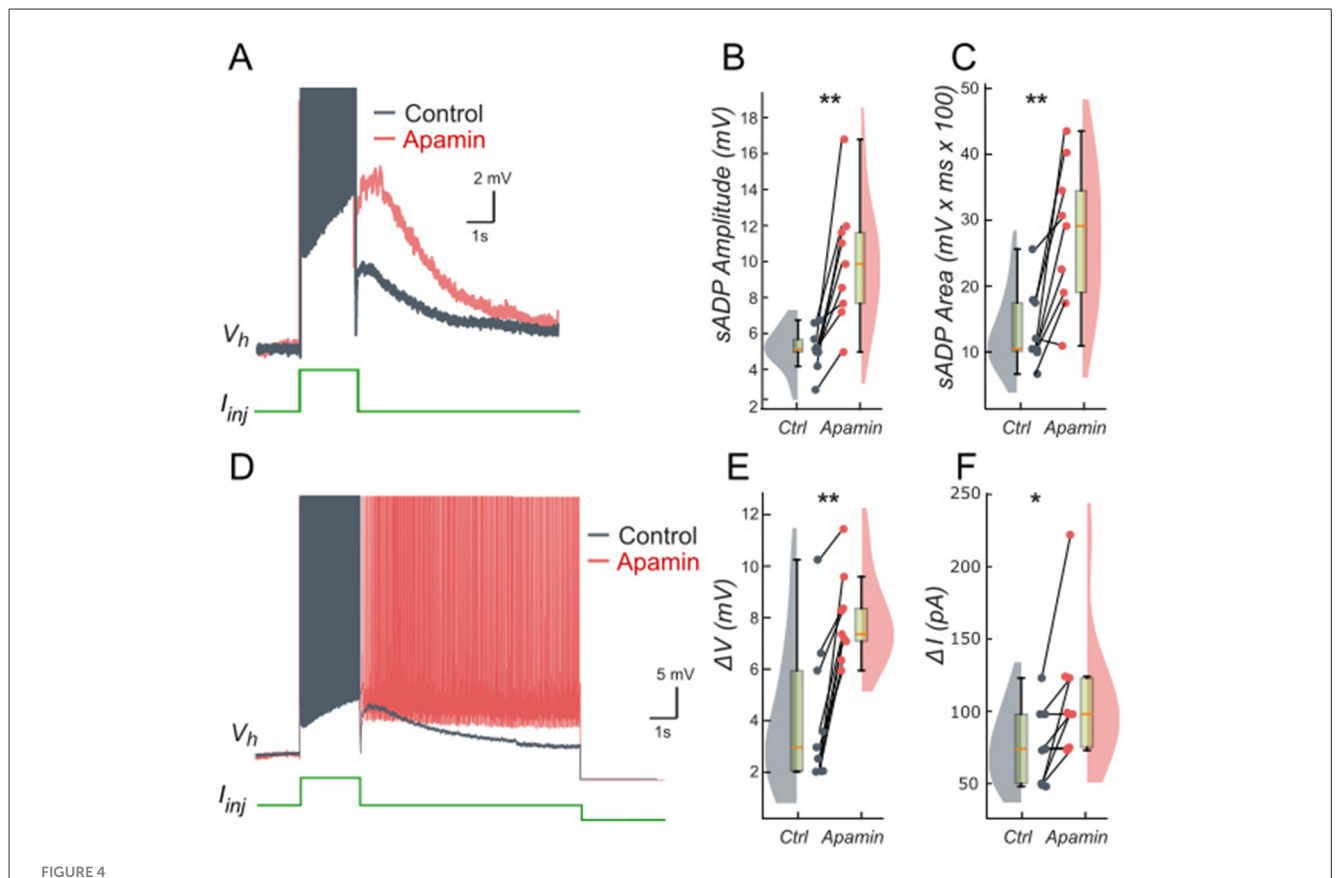
We tested these predictions pharmacologically in patch-clamp recorded lumbar motoneurons using veratridine (40 nM), which at low molar nanomolar concentrations enhances  $I_{NaP}$  (Alkadhi and Tian, 1996; Tazerart et al., 2008). Following a short depolarizing current pulse, veratridine increased the amplitude and area of the sADP (Figures 7A–C), indicating a larger depolarizing tail when  $I_{NaP}$  is enhanced. Veratridine also facilitated bistability: self-sustained spiking activity were triggered from more hyperpolarized holding potentials (Figure 7D), with Vh shifting from  $-57.5 \, \text{mV}$  (+/-9.5) to  $-62.1 \, \text{mV}$  (+/-9.0) (p < 0.01). Both the voltage range

( $\Delta V$ ) and the current range ( $\Delta I$ ) supporting bistability increased:  $\Delta V$  shifts from 3.3 mV (+/- 1.9) to 7.3 mV (+/- 2.4) (p < 0.05; Figure 7E) and  $\Delta I$  shifts from 58.5 pA (+/- 22.3) to 126.0 pA (+/-59.1) (p < 0.05; Figure 7F).

Taken together, these findings support the hypothesis that increasing  $I_{NaP}$  facilitates and broadens the operating window of  $I_{CAN}$ -driven bistability by enhancing depolarization while  $I_{CAN}$  remains the principal maintenance mechanism once engaged. This synergy between  $I_{CAN}$  and  $I_{NaP}$  helps explain how modest changes in persistent Na<sup>+</sup> conductance can markedly reshape motoneuron firing regimes.

# Bistability based on $I_{NaP}$ and the role of $[K^+]_{\circ}$

 $I_{NaP}$  could theoretically sustain bistability independently of  $I_{CAN}$  under conditions that maintain its activation between action potentials. For instance, if the inter-spike membrane



Ca<sup>2+</sup>-activated K+ current ( $I_{KCa}$ ) limits the slow afterdepolarization and membrane bistability in lumbar motoneurons. (A) Superimposed voltage traces recorded in the same motoneuron during a brief (2 s) depolarizing current step (bottom) under control conditions (black) and after bath application of apamin (200 nM; red). (B, C) Quantification of the sADP amplitude (B) and area (C). (D) Superimposed voltage traces recorded from the same holding potential (Vh) in response to a 2-s depolarizing current pulse before (black) and after apamin (red). (E, F) Quantification of bistability through  $\Delta V$  and  $\Delta I$ .  $\Delta V$  and  $\Delta I$  represent the range of holding potentials and holding currents, respectively, over which self-sustained firing can be observed. Each is defined as the difference between the most depolarized and the most hyperpolarized value (potential for  $\Delta V$ , current for  $\Delta I$ ) at which self-sustained firing is triggered or maintained (see Methods). Paired data from individual motoneurons (n = 9) are linked and overlaid on violin and box-and-whisker plots. \*P < 0.05, \*P < 0.01, two-tailed Wilcoxon signed-rank test.

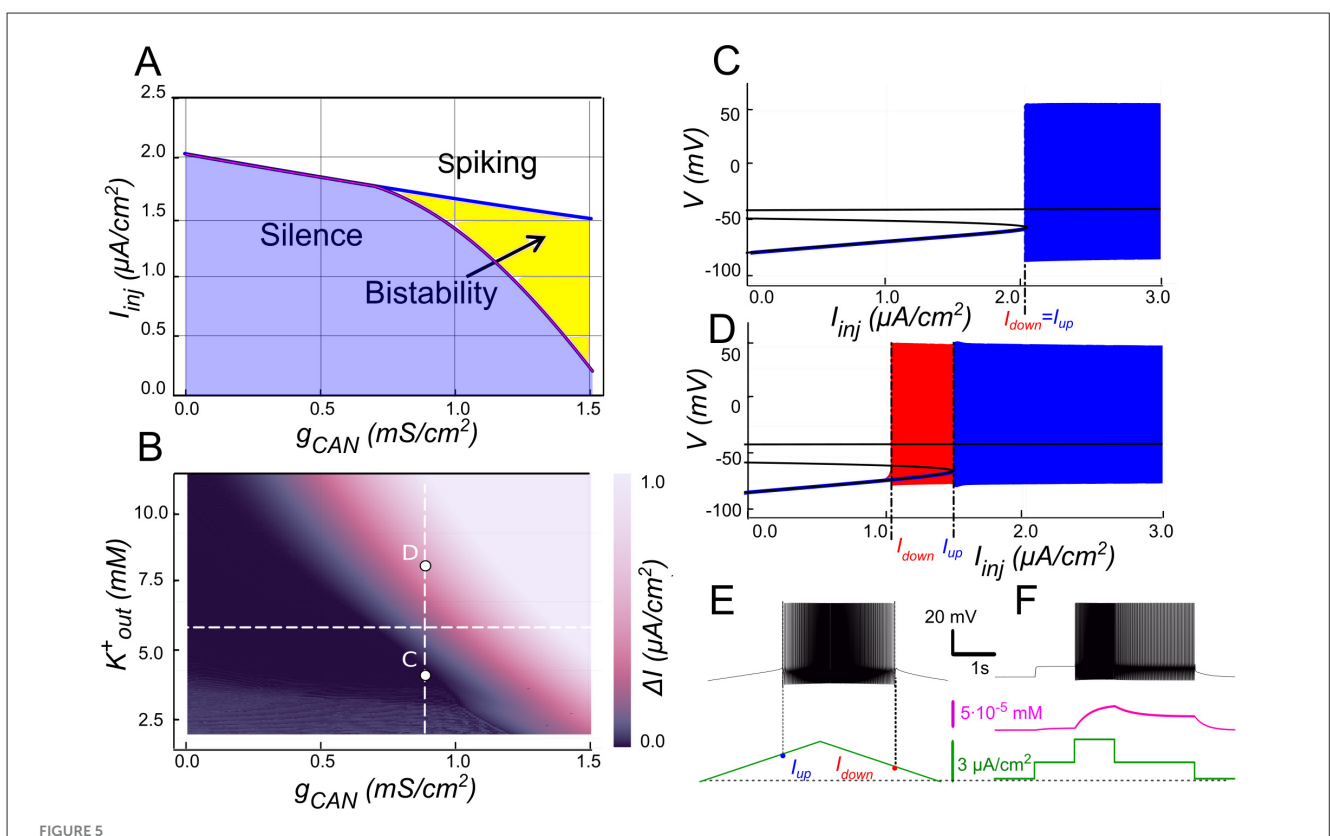
potential remains above  $I_{NaP}$ 's deactivation threshold,  $I_{NaP}$  would provide a continuous depolarizing drive, creating a self-reinforcing loop where subthreshold depolarization promotes spiking, and the resulting activity further engages  $I_{NaP}$  without full reset. Hypothetically, this mechanism might enable the neuron to toggle between quiescent and self-sustained firing states purely through sodium-based persistence, highlighting a potential alternative pathway for bistability in scenarios where calcium-dependent processes are minimized or absent.

In our model, when  $g_{CAN}=0$ ,  $I_{NaP}$  alone could not support bistability in the parameter range examined (Figure 8A). The bifurcation diagram (Figure 8D) elucidates this. At low injected current ( $I_{inj}<0.85~\mu\text{A/cm}^2$ ), the system's sole stable state is a low-voltage resting state (stable node). As  $I_{inj}$  surpasses this threshold, the node merges with a saddle point and subsequently ceases, leading to a stable limit cycle, which represents a spiking regime. A strong hyperpolarization follows each spike, dropping below the resting potential. This large post-spike hyperpolarization fully deactivates  $I_{NaP}$ , explaining its inability to maintain bistability independently. Consequently, when the injected current is decreased, the silent regime

reappears via the same bifurcation, demonstrating an absence of hysteresis.

The post-spike hyperpolarization is mediated by  $K^+$  outward currents and thus can be modulated by  $[K^+]_o$ , which sets the reversal potential  $E_K$ . Raising  $[K^+]_o$  depolarizes  $E_K$ , thereby reducing the driving force of outward currents and diminishing the post-spike hyperpolarization. Under these conditions,  $I_{NaP}$  is less completely deactivated, allowing bistability to emerge (Figures 8B, E).

As shown in Figure 8E, when  $[K^+]_o = 12 \text{ mM}$  and  $I_{inj}$  crosses a value of 0.8  $\mu$ A/cm<sup>2</sup>, the resting state is lost through the same saddle-node bifurcation, but unlike at normal  $[K^+]_o$ , the trajectory joins a pre-existing spiking limit cycle with attenuated post-spike hyperpolarization (Figures 8E, F). When  $I_{inj}$  is reduced, spiking persists down to 0.45  $\mu$ A/cm<sup>2</sup>, where the limit cycle intersects with the saddle point and disappears through a saddle-loop (homoclinic) bifurcation, and the system returns to resting state (Figures 8E, F). Thus when  $I_{inj}$  falls between 0.45 and 0.85  $\mu$ A/cm<sup>2</sup> both rest and spiking coexist, indicating a bistable regime (Figure 8G). A distinctive feature of this type of bistability is that the resting potential lies below the voltage range of the limit cycle (spiking).



Modulation of  $I_{CAN}$ -dependent bistability by extracellular potassium concentration ([K<sup>+</sup>]<sub>o</sub>). (A) Bifurcation diagram similar to Figure 3A, constructed for  $g_{KCa} = 0.5 \text{ mS/cm}^2$ , but at elevated [K<sup>+</sup>]<sub>o</sub> = 6 mM instead of physiologically normal 4 mM. Note, that compared to Figure 3A, bistability emerges at lower  $g_{CAN}$ . (B) Color-coded bistability range ( $I_{up} - I_{down}$ ) depending on  $g_{CAN}$  and [K<sup>+</sup>]<sub>o</sub>. Black area corresponds to no bistability. White dashed line shows the [K<sup>+</sup>]<sub>o</sub> value used in (A).  $g_{CAN}$  bifurcation value reduces as [K<sup>+</sup>]<sub>o</sub> increases, therefore an increase in [K<sup>+</sup>]<sub>o</sub> can lead to bistability emergence, as shown in (C, D). If  $g_{CAN} = 0.9 \text{ mS/cm}^2$ , at [K<sup>+</sup>]<sub>o</sub> = 4 mM (physiologically normal value) no bistability exists (B), but if [K<sup>+</sup>]<sub>o</sub> is raised to 8 mM, bistability emerges (C), as illustrated by ramp (E) and step (F) current protocols. (C, D) Blue indicates activity during the ascending current ramp and red indicates activity during the descending current ramp.

The presence and extent of bistable behavior depends jointly on  $g_{NaP}$  and  $[K^+]_o$ . At  $[K^+]_o = 12 \,\text{mM}$ , bistability emerges once  $g_{NaP}$  exceeds  $\sim 0.2 \,\text{mS/cm}^2$  (Figure 8B), with the current range supporting bistability expanding as  $g_{NaP}$  increases. Mapping across parameters (Figure 8C) shows that for  $g_{NaP} < 0.5 \,\text{mS/cm}^2$  bistability requires  $[K^+]_o > 10 \,\text{mM}$ ; conversely, the bistability  $g_{NaP}$  threshold decreases as  $[K^+]_o$  increases. For instance, with  $g_{NaP} = 0.25 \,\text{mS/cm}^2$ , bistability emerges once  $[K^+]_o$  exceeds  $\sim 12 \,\text{mM}$ .

Together, these results partially support the hypothesis, indicating that while under normal conditions  $I_{NaP}$  alone is insufficient to produce bistability, elevated  $[K^+]_0$  reduces outward current-mediated hyperpolarization, potentially enabling bistable firing.

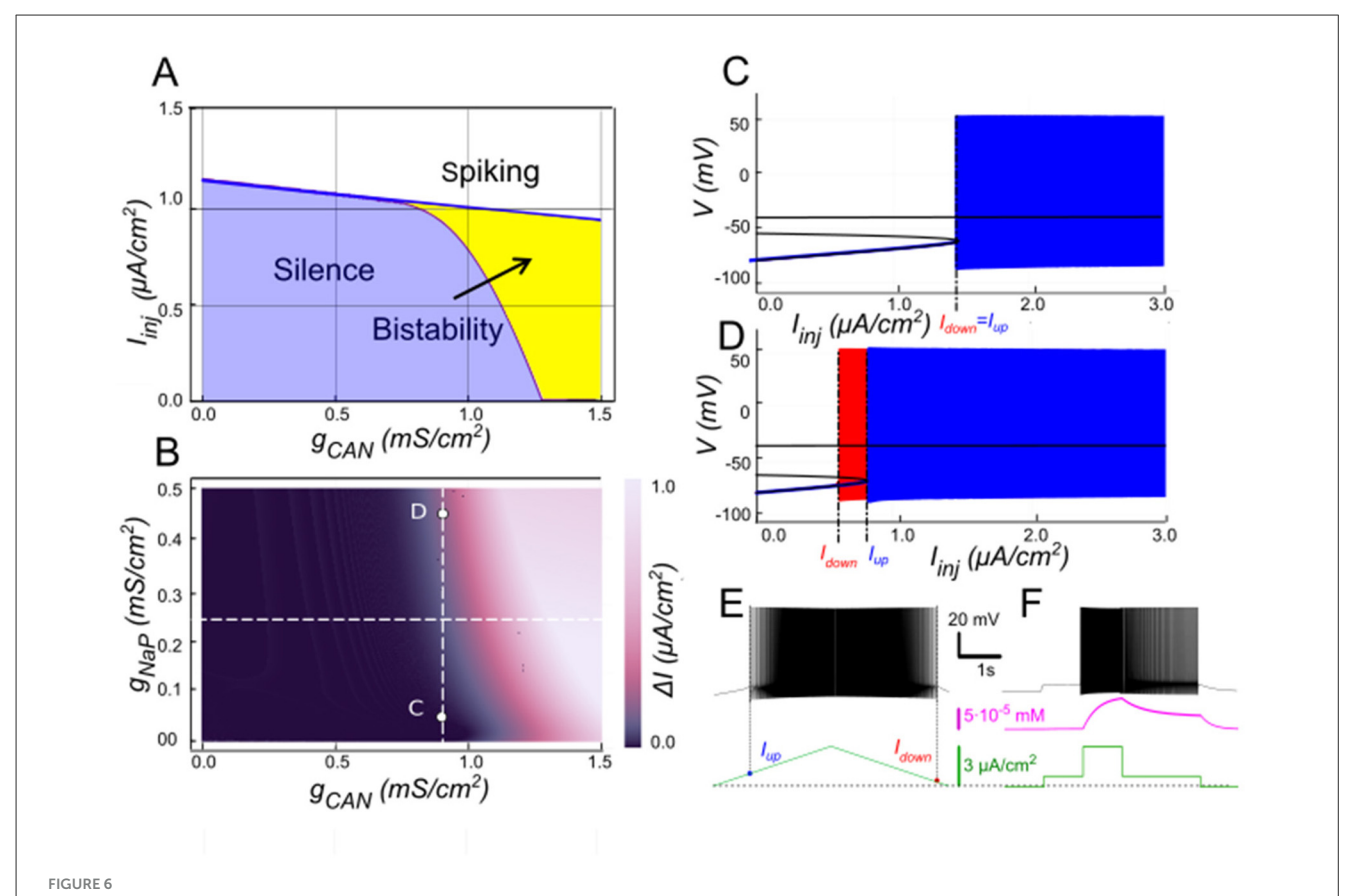
# The role of slowly inactivating potassium current $(I_{Kv1.2})$

Recent work indicates that the potassium current mediated by Kv1.2 channels ( $I_{Kv1.2}$ ) is prevalent in bistable motoneurons (Harris-Warrick et al., 2024), although its direct contribution to bistable behavior has not been fully clarified. Kv1.2 channels inactivate very slowly during repetitive firing. In principle, such

slow inactivation generates a positive feedback loop: as  $I_{Ky1.2}$  gradually decreases during ongoing spiking, the cell becomes more excitable and can persist in an active state. On the other hand, when the neuron is silent, Kv1.2 channels are fully open and  $I_{Ky1.2}$  can strongly oppose the initial depolarization. Therefore, we tested the hypotheses that  $I_{Ky1.2}$  alone can support bistability.

To clarify  $I_{KV1.2}$  contribution, we simulated our computational model while varying both  $I_{inj}$  and  $I_{KV1.2}$ 's maximal conductance,  $g_{KV1.2}$ . In these simulations,  $I_{KV1.2}$  alone did not produce bistability between resting and spiking states thus invalidating the hypothesis. Instead, the model generated a regime of periodic bursting, alternating between spiking and quiescent phases, over an extremely narrow range of  $I_{inj}$ .

A signature of  $I_{K\nu 1.2}$  is its effect on firing dynamics during constant depolarization: rather than stabilizing tonic firing, it induced a delayed excitation with ramping spike frequency (Bos et al., 2018). To isolate this effect, we removed both  $I_{CAN}$  and  $I_{NaP}$  ( $g_{NaP}=g_{CAN}=0$ ). Under these conditions (Figure 9B), a rectangular current pulse elicited an initial fast depolarization followed by a slow secondary depolarization. If the stimulus was strong enough, this slow drift brought the neuron to a spiking threshold and then spiking began, with the firing rate progressively accelerating. This behavior reflects very slow inactivation kinetics of  $I_{K\nu 1.2}$ . Initially,  $I_{K\nu 1.2}$  activates quickly, temporarily opposing



Modulation of  $I_{CAN}$ -dependent bistability by  $I_{NaP}$ . (A) Bifurcation diagram similar to Figure 3A, constructed for  $g_{KCa} = 0.5 \text{ mS/cm}^2$ , but at  $g_{NaP} = 0.25 \text{ mS/cm}^2$  instead of zero. Note, that compared to Figure 3A, bistability emerges at lower  $g_{CAN}$ . (B) Color-coded bistability range  $(I_{up} - I_{down})$  depending on  $g_{CAN}$  and  $g_{NaP}$  with  $g_{KCa}$  fixed at 0.5 mS/cm<sup>2</sup>. Black area corresponds to no bistability.  $g_{CAN}$  bifurcation value reduces as  $g_{NaP}$  increases, therefore an increase in  $g_{NaP}$  can lead to bistability emergence, as shown in (C, D) where blue indicates activity during the ascending current ramp and red indicates activity during the descending current ramp. If  $g_{CAN} = 0.9 \text{ mS/cm}^2$ , at  $g_{NaP} = 0$  no bistability exists (C), but if  $g_{NaP}$  is raised to 0.45 mS/cm<sup>2</sup>, bistability emerges (D), as illustrated by ramp (E) and step current protocols (F).

depolarization, but then inactivates with a time constant of  $\sim$ 2.5 s (see Methods), progressively reducing its own inhibitory effect and permitting further depolarization and firing.

By contrast, in absence of  $I_{Kv1.2}$  but with  $I_{KCa}$  present, the model showed spike frequency adaptation (Figure 9A). Here, firing decreased over time because  $I_{KCa}$  hyperpolarized the membrane. When both currents ( $I_{Kv1.2}$  and  $I_{KCa}$ ) were present, the firing dynamics (whether it shows ramping or adaptation) depended on their relative balance. This interaction can lead to complex dynamics where the slow inactivation of  $I_{Kv1.2}$  competes with the calcium-dependent potassium currents tendency to stabilize or reduce firing frequency.

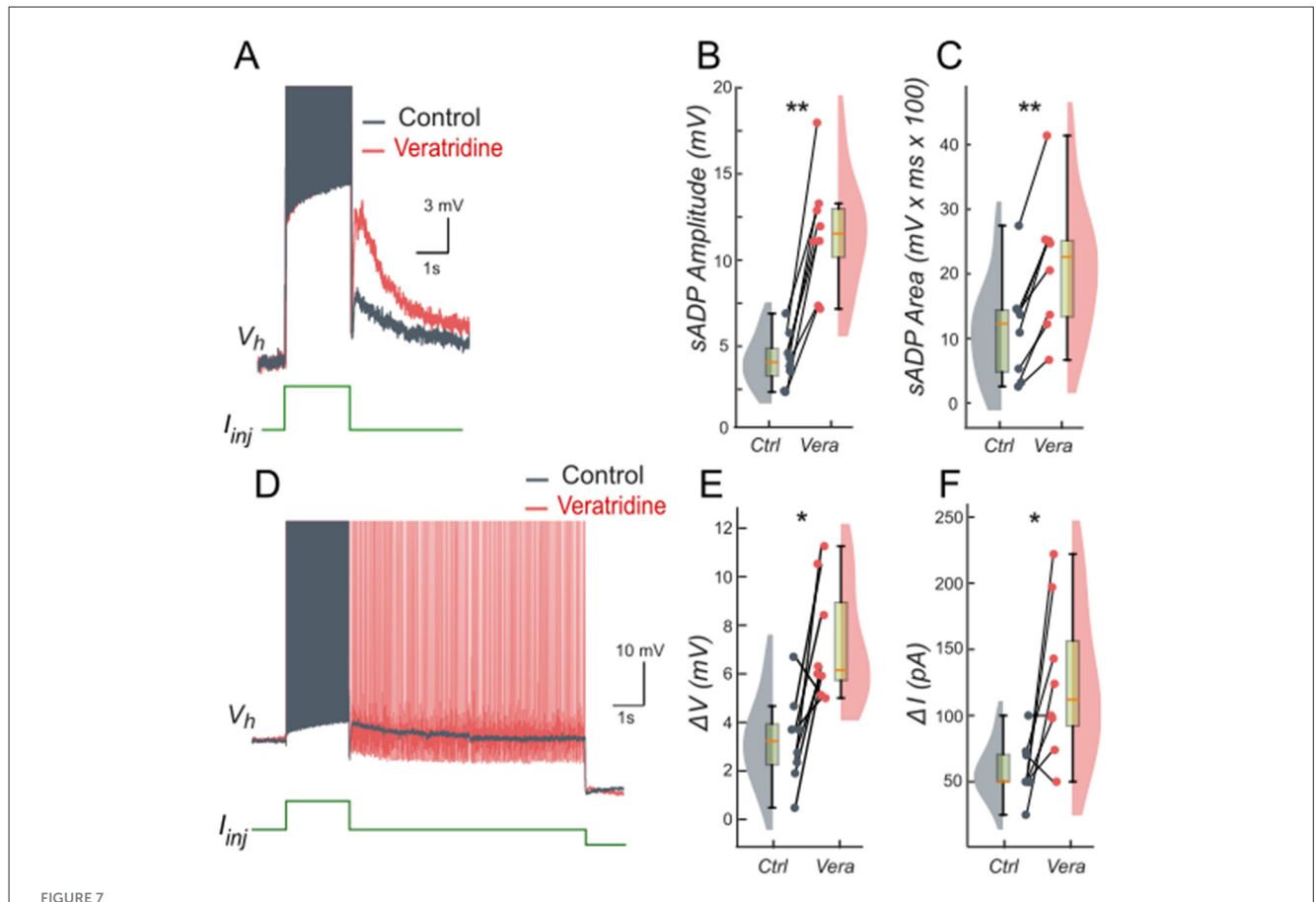
# Discussion

In this study, we used a single-compartment computational model of spinal motoneurons to dissect the ionic mechanisms underlying bistability. Our results identify a minimal core mechanism based on the synergistic interactions among  $I_{CaL}$ , CICR, and  $I_{CAN}$  strongly modulated by  $I_{KCa}$ ,  $I_{NaP}$  and  $[K^+]_o$ . These findings offer new insights into how bistable firing is generated and regulated in motoneurons.

# Motoneuron bistability critically depends on the $I_{CaL}$ -CICR- $I_{CAN}$ loop

Early studies attributed plateau potentials and bistability to persistent L-type calcium currents (Schwindt and Crill, 1980; Hounsgaard et al., 1988a,b; Hounsgaard and Mintz, 1988; Hounsgaard and Kiehn, 1989; Hounsgaard and Kjaerulff, 1992; Svirskis and Hounsgaard, 1997), a view reinforced by computational models requiring dendritic  $I_{CaL}$  to replicate these bistable behaviors (Booth and Rinzel, 1995; Booth et al., 1997; Carlin et al., 2000; ElBasiouny et al., 2005; Bui et al., 2006; Carlin et al., 2009; Kim and Jones, 2011). Immunohistochemical data further supported this interpretation by revealing the dendritic distribution of L-type Cav1.3 channels (Simon et al., 2003; Zhang et al., 2008). More recent findings have revealed a complementary mechanism, in which  $I_{CaL}$  primarily acts as a trigger, while other currents, notably the ICAN, play a central role in mediating plateau potentials and bistability (Bos et al., 2021), as observed in motoneurons from neonatal and young adult murine models (Harris-Warrick et al., 2024).

Our computational findings reinforce and extend this view. The model shows that initial  $Ca^{2+}$  entry through  $I_{CaL}$  is insufficient to sustain bistability due to fast  $Ca^{2+}$  removal from the cytosol. The



Persistent Na<sup>+</sup> current ( $I_{NaP}$ ) facilitates the slow afterdepolarization and membrane bistability in lumbar motoneurons. (**A**) Superimposed voltage traces recorded in the same motoneuron during a brief (2 s) depolarizing current step (bottom) under control conditions (black) and after bath application of veratridine (40 nM; red). (**B**, **C**) Quantification of the sADP amplitude (**B**) and area (**C**). (**D**) Superimposed voltage traces recorded from the same holding potential (Vh = -65 mV) in response to a 2-s depolarizing current pulse before (black) and after (red) veratridine. (**E**, **F**) Quantification of bistability through  $\Delta V$  and  $\Delta I$ .  $\Delta V$  and  $\Delta I$  represent the range of holding potentials and holding currents, respectively, over which self-sustained firing can be observed. Each is defined as the difference between the most depolarized and the most hyperpolarized value (potential for  $\Delta V$ , current for  $\Delta I$ ) at which self-sustained firing is triggered or maintained (see Methods). Paired data from individual motoneurons (n = 8) are linked and overlaid on violin and box-and-whisker plots. \*P < 0.05, \*\*P < 0.01, two-tailed Wilcoxon signed-rank test.

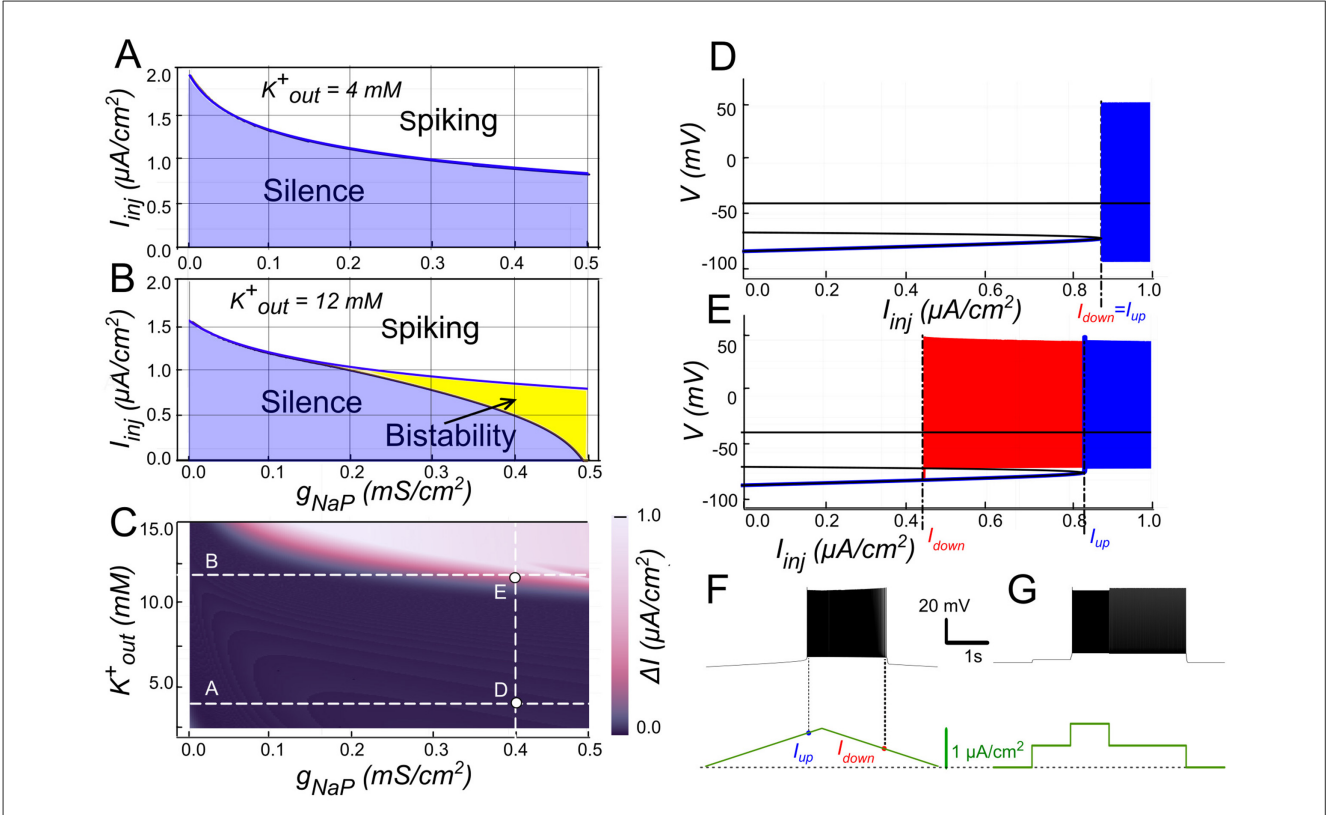
necessary amplification arises from CICR, linking  $I_{CaL}$ -mediated Ca<sup>2+</sup> influx to intracellular stores. Accordingly, CICR surpasses the capacity of Ca<sup>2+</sup> pumps to rapidly clear cytoplasmic Ca<sup>2+</sup>, and therefore enables sustained intracellular Ca<sup>2+</sup>, long-lasting  $I_{CAN}$  activation and bistability. Consistent with this, motoneuron bistability is abolished when CICR is inhibited, even though  $I_{CaL}$  currents are still present (Bouhadfane et al., 2013; Bos et al., 2021; Harris-Warrick et al., 2024). Together,  $I_{CaL}$ , CICR, and  $I_{CAN}$  emerge from the findings as a functional triad instrumental in motoneuron bistability. As such, the triad may provide a general feed-forward mechanism for plateau generation across different structures of the CNS, owing to the fact that  $I_{CAN}$  also supports motor, sensory and memory-related plateaus (Fraser and MacVicar, 1996; Morisset and Nagy, 1999; Di Prisco et al., 2000; Yan et al., 2009; Toporikova and Butera, 2011; Jasinski et al., 2013).

# Suppression of $I_{\text{CAN}}$ -based bistability by $I_{\text{KCa}}$

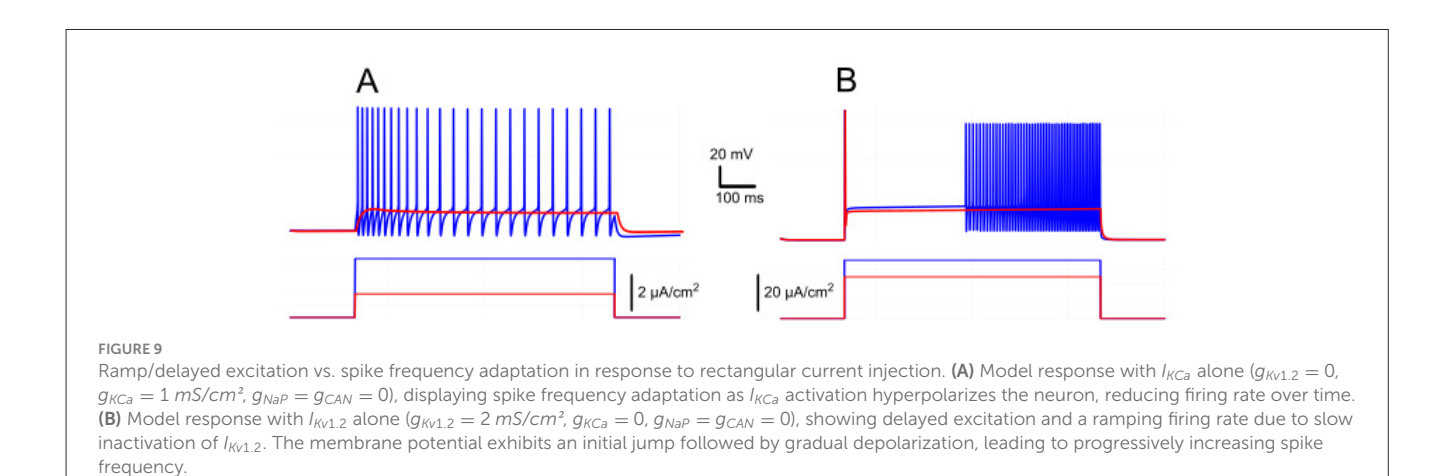
The model adds a key regulatory layer to motoneuron bistability by clarifying the interplay between  $I_{CAN}$  and  $I_{KCa}$ .

I<sub>KCa</sub> dominance, thought to be driven by Ca<sup>2+</sup> influx through dendritic L-type calcium channels (Mousa and Elbasiouny, 2020) inhibits  $I_{CAN}$ -driven plateaus and prevents their formation. In line with the model, reducing  $I_{KCa}$  with apamin facilitates the expression of bistability and can unmask latent plateau potentials (Hounsgaard and Mintz, 1988; Hounsgaard and Kiehn, 1993). The relative contributions of  $I_{CAN}$  and  $I_{KCa}$  may tune the propensity to bistability across motoneuron subtypes. Bistability appears more frequently observed in large motoneurons (Harris-Warrick et al., 2024), a finding that, according to the assumption, would reflect a higher  $I_{CAN}/I_{KCa}$  ratio. This interpretation aligns with established physiological distinctions where large motoneurons, in line with size-dependent differential expression of SK channels (Deardorff et al., 2013), display brief AHPs, whereas small motoneurons exhibit prolonged AHPs (Kernell, 1965; Gustafsson and Pinter, 1984). In addition, large motoneurons generate stronger  $I_{CAN}$  than small motoneurons (Harris-Warrick et al., 2024).

Our model also identifies  $[K^+]_o$  as a critical factor influencing  $I_{KCa}$  efficacy. Elevating  $[K^+]_o$  depolarizes  $E_K$ , weakening  $I_{KCa}$  and shifting the balance toward  $I_{CAN}$ , thereby enhancing bistability (Figure 4). Disruption of  $K^+$  buffering through astrocytic Kir4.1 dysfunction in spinal cord injury (Olsen et al., 2010; Benson et al.,



Bistability based on  $I_{NaP}$  and the role of  $[K^+]_o$ . (A) Activity regimes of the model neuron depending on the injected current  $(I_{inj})$  and the conductance of persistent sodium current  $(g_{NaP})$  at baseline  $K^+$  extracellular concentration  $([K^+]_o = 4 \text{ mM})$ . At all values of  $g_{NaP}$  as the injected current changes, the model transitions from silence to spiking and back with no hysteresis which indicates no bistability. (B) Activity patterns of the model neuron depending on the injected current and  $g_{NaP}$  conductance at  $[K^+]_o = 12 \text{ mM}$ . Once  $g_{NaP}$  exceeds approximately 0.15 mS/cm², bistability emerges. (C) Adjusting the sodium persistent inward current  $(I_{NaP})$  conductance  $(g_{NaP})$  and extracellular potassium concentration  $([K^+]_o)$  in a model neuron reveals bistable regimes. The range of injected current where bistability occurs is shown in color, with black indicating no bistability. Higher  $[K^+]_o$  levels require smaller  $g_{NaP}$  for bistability, suggesting that increased  $[K^+]_o$  can induce bistability in neurons with otherwise insufficient  $g_{NaP}$  expression. (D) At  $g_{NaP} = 0.4 \text{ mS/cm}^2$  and  $[K^+]_o = 4 \text{ mM}$  no bistability is observed. (E) However, as  $[K^+]_o$  is increased to 12 mM, bistability emerges, as illustrated by ramp (F) and step current protocols (G). (D, E) Blue indicates activity during the ascending current ramp and red indicates activity during the descending current ramp.



2023; Barbay et al., 2025), is likely to elevate  $[K^+]_o$ , paralleling findings from epilepsy studies (Djukic et al., 2007; Tong et al., 2014). A subsequent shift toward  $I_{CAN}$  is predicted to strengthen bistability and worsen spasticity (Bennett et al., 2001; Brocard et al., 2016).

# Facilitation of $I_{\text{CAN}}$ -mediated bistability by $I_{\text{NaP}}$

While  $I_{CAN}$  is the main driver of bistability,  $I_{NaP}$  acts as an essential modulator, extending the conditions under which

bistability occurs. In our simulations, increasing  $I_{NaP}$  lowers the threshold for I<sub>CAN</sub>-mediated bistability, enabling sustained firing even when  $I_{CAN}$  alone is insufficient (Figure 6). Due to subthreshold depolarization (Crill, 1996) that enables repetitive spiking (Kuo et al., 2006), I<sub>NaP</sub> biases the system toward I<sub>CaL</sub>-CICR-I<sub>CAN</sub> engagement and plateau generation. In line with this role, riluzole, an established inhibitor of  $I_{NaP}$ , reliably suppresses selfsustained firing in bistable motoneurons (Bouhadfane et al., 2013; Drouillas et al., 2023). At first glance, this might imply that plateau potentials depend directly on  $I_{NaP}$ . However, the persistence of TTX-resistant sADP after rizulole application (Bouhadfane et al., 2013; Drouillas et al., 2023) suggests that  $I_{CAN}$  provides the essential substrate for bistable behavior, while  $I_{NaP}$  serves as a facilitator. The  $I_{NaP}$  and  $I_{CAN}$  interaction extends beyond motoneurons; in the preBotzinger complex, for example, the two currents cooperate to produce rhythmic bursting (Jasinski et al., 2013; Phillips et al., 2019, 2022).

Under physiological conditions,  $I_{NaP}$  alone unlikely supports bistability because hyperpolarizing potassium currents deactivate  $I_{NaP}$  between spikes (Figure 8). Elevating  $[K^+]_0$  mitigates this hyperpolarization by depolarizing  $E_K$ , and allows  $I_{NaP}$  to create bistability at higher  $g_{NaP}$  (Figure 8C). This has been clearly demonstrated in our simulations, where a pure  $I_{NaP}$ -based bistability emerges as  $[K^+]_0$  approaches or exceeds 12 mM. This scenario may be relevant in spinal cord injury (SCI), where  $I_{NaP}$  is enhanced (Bennett et al., 2001; Li et al., 2004; Harvey et al., 2006; Brocard et al., 2016). In conjunction with high  $[K^+]_0$ , this enhancement can strengthen bistability and promote spasticity. Consequently, riluzole (Rilutek $^{\textcircled{e}}$ ), originally developed for amyotrophic lateral sclerosis (ALS), is being explored to target spasticity in SCI patients (Cotinat et al., 2023).

# The role of slowly inactivating potassium current $(I_{Kv1.2})$

In spinal motoneurons,  $I_{Kv1.2}$  imposes an initial brake on excitability and then relaxes over seconds, yielding delayed spiking and a characteristic ramping of discharge during sustained depolarization (Bos et al., 2018). Because this property scales with motoneuron size, larger α-motoneurons show stronger delayed excitation and ramping (Harris-Warrick et al., 2024). Yet, despite the greater prevalence of bistability in larger motoneurons, evidence for a generative role of Kv1.2 remains elusive. Our simulations clarify this point. Varying  $I_{Kv1.2}$ in isolation never produced robust switching between silent and self-sustained firing states. Instead, it generated narrow-band bursting around a tight input window, while the hallmark hysteresis of bistability was absent. Mechanistically,  $I_{Kv1.2}$  lacks the positive feedback needed to maintain a depolarized upstate. It is an outward conductance that weakens with use, modulating access to the plateau regime but not providing the sustaining inward drive. In contrast, stable bistability in both our model and experiments requires the  $I_{CaL}$ -CICR-  $I_{CAN}$ triad, a view reinforced by the identification of Trpm5 as the principal  $Na^+$ -permeable carrier of  $I_{CAN}$  underlying motoneuron plateaus (Bos et al., 2021). When TRPM5/ $I_{CAN}$  is suppressed, slow after depolarization and plateaus collapse even though  $I_{Kv1.2}$  is intact, directly demonstrating that Kv1.2 is permissive rather than generative for bistability.

# Serotonin and bistability

Brainstem-derived monoamines are central to motoneuron excitability and bistability (Heckman et al., 2008). In decerebrate cats, bistability depends on descending monoaminergic drive (Conway et al., 1988; Hounsgaard et al., 1988a; Lee and Heckman, 1998b, 1999). Acute spinalization removes these inputs and thereby reduces bistable properties of motoneurons, whereas monoamine reintroduction restores plateau potentials (Hounsgaard et al., 1988a). Among these modulators, serotonin is especially effective. In vertebrates, exogenous serotonin enhances excitability and bistability (Hounsgaard and Kiehn, 1985, 1989).

Mechanistically, serotonin acts primarily through 5-HT<sub>2</sub> receptors to amplify ionic currents that promote bistability. By increasing dendritic L-type calcium currents (Hounsgaard and Kiehn, 1989; Perrier and Hounsgaard, 2003; Perrier and Delgado-Lezama, 2005; Perrier and Cotel, 2008) it can promote calcium build-up and  $I_{CAN}$  activation as described in our model. Serotonin also shifts  $I_{NaP}$  activation toward hyperpolarized potentials, thereby amplifying neuronal excitability (Li and Bennett, 2003; Harvey et al., 2006). The shift enhances I<sub>NaP</sub> and thus facilitates  $I_{CAN}$ -mediated bistability. Finally, serotonin also reduces outward currents, notably  $I_{KCa}$ , thereby facilitating high-frequency firing (Grunnet et al., 2004). This serotoninevoked reduction of IKCa may lead to bistability in spinal motoneurons (Hounsgaard et al., 1988b; Hounsgaard and Kiehn, 1993), as demonstrated in our present modeling and experimental results.

The role of serotonin becomes especially evident during SCI, not because of its direct action, but rather because of its sudden loss following disruption of descending inputs. Initial serotonin depletion produces motoneurons hypofunction, otherwise known as "spinal shock" (Schadt and Barnes, 1980), mirroring the loss of bistability in our model upon blockade of  $I_{CAN}$  or CICR. However, with time, excitability and plateau potentials re-emerge, representing an electrophysiological correlate of chronic spasticity and hyperreflexia (Bennett et al., 2001). The rebound is attributed to plasticity in serotonin receptor signaling. Most notably, 5-HT<sub>2B</sub> and 5-HT<sub>2C</sub> receptors become constitutively active which restores persistent inward currents (e.g., INAP) and plateau firing even without serotonergic input (Li and Bennett, 2003; Murray et al., 2010, 2011; D'Amico et al., 2013; Tysseling et al., 2017). Consistent with this, our model shows that increased  $I_{NaP}$  strengthens  $I_{CAN}$ driven bistability.

# Limitations and future research directions

Dendritic calcium currents have been repeatedly linked to motoneuron plateaus and bistability (Booth et al., 1997; Carlin et al., 2000; Simon et al., 2003; ElBasiouny et al., 2005; Bui et al., 2006; Zhang et al., 2008). Our single-compartment computational

model reproduces key features of motoneuron bistability, yet its simplified architecture cannot capture the full spatial complexity of motoneurons. By collapsing dendrites into one compartment, our results indicate that a simplified representation can nevertheless sustain bistability (Booth et al., 1997; Carlin et al., 2000; ElBasiouny et al., 2005; Bui et al., 2006) Indeed, dendritic  $I_{CaL}$  may amplify calcium signaling and could shape the expression and robustness of plateaus. On the other hand, this simplification does not preclude physiological relevance, as somatic L-type calcium channels can themselves generate prolonged tail currents in motoneurons (Moritz et al., 2007). Such findings support the view that critical aspects of motoneuron bistability can also emerge from intrinsic soma-based mechanisms.

Our future work will thus include the construction and use of multi-compartment models to explore the role of spatial distribution of  $I_{CaL}$ , CICR, and  $I_{CAN}$  for testing how dendritevs. soma-localized mechanisms affect bistability. In this context, establishing the precise subcellular localization of  $I_{CAN}$  channels remains a priority but progress is limited by the lack of highly specific antibodies to TRPM5, the presumed molecular correlate of  $I_{CAN}$  (Bos et al., 2021). Our analysis centers at L-type calcium channels only, but motoneurons also express T-type and N-type calcium channels (Umemiya and Berger, 1995; Hivert et al., 1995; Viana et al., 1997). Since these currents can complement or replace L-type currents in generating plateaus (Bouhadfane et al., 2013), future models may be instrumental in evaluating their contributions.

In addition to SK-mediated AHPs, motoneurons also display an ultra-slow afterhyperpolarization (usAHP) generated by the electrogenic Na<sup>+</sup>/K<sup>+</sup>-ATPase pump. This current, activated by intracellular Na<sup>+</sup> accumulation during repetitive firing, produces a long-lasting hyperpolarization that transiently decreases motoneuron excitability. Such pump-mediated usAHPs have been described in lumbar motoneurons (Picton et al., 2017a,b; Sharples et al., 2025). Although not included in the present model, it would be interesting to test in future work how the inclusion of a Na<sup>+</sup>/K<sup>+</sup>-pump component could influence plateau potentials and bistability in motoneurons.

In summary, our minimal model captures the core features of bistable firing, with the  $I_{CaL}$ -CICR- $I_{CAN}$  triad emerging as a central mechanism, while leaving open the contribution of dendritic processes. Future anatomically detailed models and experiments will be needed to resolve the effects of channels' spatial distributions across motoneuron compartments.

# Data availability statement

The datasets presented in this study can be found in online repositories. The names of the repository/repositories and accession number(s) can be found at: https://doi.org/10.5281/zenodo.15527835.

# **Ethics statement**

The animal study was approved by Comité d'Ethique en Neurosciences INT-Marseille, CE71 Nb A1301404, authorization

Nb 2018110819197361. The study was conducted in accordance with the local legislation and institutional requirements.

## **Author contributions**

YM: Conceptualization, Data curation, Formal analysis, Investigation, Methodology, Project administration, Resources, Software, Supervision, Validation, Visualization, Writing - original draft, Writing - review & editing. FK: Data curation, Formal analysis, Investigation, Validation, Visualization, Writing - review & editing. RJ: Formal analysis, Investigation, Software, Supervision, Validation, Visualization, Writing - review & editing. TS: Software, Visualization, Writing - review & editing. MM: Investigation, Software, Visualization, Writing - review & editing. FB: Conceptualization, Formal analysis, Funding acquisition, Investigation, Methodology, Project administration, Resources, Supervision, Validation, Visualization, Writing - original draft, Writing - review & editing. IR: Conceptualization, Formal analysis, Funding acquisition, Investigation, Methodology, Project administration, Resources, Supervision, Visualization, Writing original draft, Writing - review & editing.

# **Funding**

The author(s) declare that financial support was received for the research and/or publication of this article. This work was supported by the ANR MotoBis grant (ANR-24-CE16-1548-01) to FB and the NIH/NINDS grant (R01 NS130799) to IR.

# Conflict of interest

The authors declare that the research was conducted in the absence of any commercial or financial relationships that could be construed as a potential conflict of interest.

## Generative Al statement

The author(s) declare that Gen AI was used in the creation of this manuscript. The authors used an AI tool exclusively for grammar and phrasing purposes.

Any alternative text (alt text) provided alongside figures in this article has been generated by Frontiers with the support of artificial intelligence and reasonable efforts have been made to ensure accuracy, including review by the authors wherever possible. If you identify any issues, please contact us.

## Publisher's note

All claims expressed in this article are solely those of the authors and do not necessarily represent those of their affiliated organizations, or those of the publisher, the editors and the reviewers. Any product that may be evaluated in this article, or claim that may be made by its manufacturer, is not guaranteed or endorsed by the publisher.

# References

- Alkadhi, K. A., and Tian, L. M. (1996). Veratridine-enhanced persistent sodium current induces bursting in CA1 pyramidal neurons. *Neuroscience* 71, 625–632. doi:10.1016/0306-4522(95)00488-2
- Barbay, T., Pecchi, E., Ramirez-Franco, J., Ivanov, A., Brocard, F., Rouach, N., et al. (2025). Functional contribution of astrocytic Kir4.1 channels to spasticity after spinal cord injury. *Brain* 48:awaf147. doi: 10.1101/2024.10.11.617793
- Bennett, D. J., Li, Y., and Siu, M. (2001). Plateau potentials in sacrocaudal motoneurons of chronic spinal rats, recorded *in vitro*. *J. Neurophysiol*. 86, 1955–1971. doi: 10.1152/jn.2001.86.4.1955
- Benson, C. A., King, J. F., Kauer, S. D., Waxman, S. G., and Tan, A. M. (2023). Increased astrocytic GLT-1 expression in tripartite synapses is associated with SCI-induced hyperreflexia. *J. Neurophysiol.* 130, 1358–1366. doi: 10.1152/jn.00234.2023
- Binder, M. D., Powers, R. K., and Heckman, C. J. (2020). Non-linear input-output functions of motoneurons. *Physiology* 35, 31–39. doi: 10.1152/physiol.00026.2019
- Boost Development Team (n.d.). Boost C++ libraries (Version 1.86). (ver. 1.86). [C++]. Available online at: https://www.boost.org/ (Accessed October 27, 2025).
- Booth, V., and Rinzel, J. (1995). A minimal, compartmental model for a dendritic origin of bistability of motoneuron firing patterns. *J. Comput. Neurosci.* 2, 299–312. doi: 10.1007/BF00961442
- Booth, V., Rinzel, J., and Kiehn, O. (1997). Compartmental model of vertebrate motoneurons for Ca<sup>2+</sup>-dependent spiking and plateau potentials under pharmacological treatment. *J. Neurophysiol.* 78, 3371–3385. doi: 10.1152/jn.1997.78.6.3371
- Bos, R., Drouillas, B., Bouhadfane, M., Pecchi, E., Trouplin, V., Korogod, S. M., et al. (2021). Trpm5 channels encode bistability of spinal motoneurons and ensure motor control of hindlimbs in mice. *Nat. Commun.* 12:6815. doi: 10.1038/s41467-021-27113-x
- Bos, R., Harris-Warrick, R. M., Brocard, C., Demianenko, L. E., Manuel, M., Zytnicki, D., et al. (2018). Kv1.2 Channels promote non-linear spiking motoneurons for powering up locomotion. *Cell Rep.* 22, 3315–3327. doi: 10.1016/j.celrep.2018.02.093
- Bouhadfane, M., Tazerart, S., Moqrich, A., Vinay, L., and Brocard, F. (2013). Sodium-mediated plateau potentials in lumbar motoneurons of neonatal rats. *J. Neurosci.* 33, 15626–15641. doi: 10.1523/JNEUROSCI.1483-13.2013
- Brocard, C., Plantier, V., Boulenguez, P., Liabeuf, S., Bouhadfane, M., Viallat-Lieutaud, A., et al. (2016). Cleavage of Na+ channels by calpain increases persistent Na+ current and promotes spasticity after spinal cord injury. *Nat. Med.* 22, 404–411. doi: 10.1038/nm.4061
- Brocard, F., Shevtsova, N. A., Bouhadfane, M., Tazerart, S., Heinemann, U., Rybak, I. A., et al. (2013). Activity-dependent changes in extracellular Ca2+ and K+ reveal pacemakers in the spinal locomotor-related network. *Neuron* 77, 1047–1054. doi: 10.1016/j.neuron.2013.01.026
- Bui, T. V., Ter-Mikaelian, M., Bedrossian, D., and Rose, P. K. (2006). Computational estimation of the distribution of L-type Ca(2+) channels in motoneurons based on variable threshold of activation of persistent inward currents. *J. Neurophysiol.* 95, 225–241. doi: 10.1152/jn.00646.2005
- Carlin, K. P., Bui, T. V., Dai, Y., and Brownstone, R. M. (2009). Staircase currents in motoneurons: insight into the spatial arrangement of calcium channels in the dendritic tree. *J. Neurosci.* 29, 5343–5353. doi: 10.1523/JNEUROSCI.5458-08.2009
- Carlin, K. P., Jones, K. E., Jiang, Z., Jordan, L. M., and Brownstone, R. M. (2000). Dendritic L-type calcium currents in mouse spinal motoneurons: implications for bistability. *Eur. J. Neurosci.* 12, 1635–1646. doi: 10.1046/j.1460-9568.2000.00055.x
- Collins, D. F., Burke, D., and Gandevia, S. C. (2001). Large involuntary forces consistent with plateau-like behavior of human motoneurons. *J. Neurosci.* 21, 4059–4065. doi: 10.1523/JNEUROSCI.21-11-04059.2001
- Conway, B. A., Hultborn, H., Kiehn, O., and Mintz, I. (1988). Plateau potentials in alpha-motoneurones induced by intravenous injection of L-dopa and clonidine in the spinal cat. *J. Physiol.* 405, 369–384. doi: 10.1113/jphysiol.1988.sp017337
- Cotinat, M., Boquet, I., Ursino, M., Brocard, C., Jouve, E., Alberti, C., et al. (2023). Riluzole for treating spasticity in patients with chronic traumatic spinal cord injury: study protocol in the phase ib/iib adaptive multicenter randomized controlled RILUSCI trial. *PLoS ONE* 18:e0276892. doi: 10.1371/journal.pone.0276892
- Crill, W. E. (1996). Persistent sodium current in mammalian central neurons. *Annu. Rev. Physiol.* 58, 349–362. doi: 10.1146/annurev.ph.58.030196.002025
- D'Amico, J. M., Murray, K. C., Li, Y., Chan, K. M., Finlay, M. G., Bennett, D. J., et al. (2013). Constitutively active 5-HT2/ $\alpha$ 1 receptors facilitate muscle spasms after human spinal cord injury. *J. Neurophysiol.* 109, 1473–1484. doi: 10.1152/jn.00821.2012
- Deardorff, A. S., Romer, S. H., Deng, Z., Bullinger, K. L., Nardelli, P., Cope, T. C., et al. (2013). Expression of postsynaptic Ca2+-activated K+ (SK) channels at C-bouton synapses in mammalian lumbar-motoneurons. *J. Physiol.* 591, 875–897. doi: 10.1113/jphysiol.2012.240879
- Di Prisco, G. V., Pearlstein, E., Le Ray, D., Robitaille, R., and Dubuc, R. (2000). A cellular mechanism for the transformation of a sensory input into a motor command. *J. Neurosci.* 20, 8169–8176. doi: 10.1523/JNEUROSCI.20-21-08169.2000

- Djukic, B., Casper, K. B., Philpot, B. D., Chin, L. S., and McCarthy, K. D. (2007). Conditional knock-out of Kir4.1 leads to glial membrane depolarization, inhibition of potassium and glutamate uptake, and enhanced short-term synaptic potentiation. *J. Neurosci.* 27, 11354–11365. doi: 10.1523/JNEUROSCI.0723-07.2007
- Drouillas, B., Brocard, C., Zanella, S., Bos, R., and Brocard, F. (2023). Persistent Nav1.1 and Nav1.6 currents drive spinal locomotor functions through non-linear dynamics. *Cell Rep.* 42:113085. doi: 10.1016/j.celrep.2023.113085
- Eken, T., Hultborn, H., and Kiehn, O. (1989). Possible functions of transmitter-controlled plateau potentials in alpha motoneurones. *Progr. Brain Res.* 80, 257–267; discussion 239-242. doi: 10.1016/S0079-6123(08)62219-0
- Eken, T., and Kiehn, O. (1989). Bistable firing properties of soleus motor units in unrestrained rats. *Acta Physiol. Scand.* 136, 383–394. doi: 10.1111/j.1748-1716.1989.tb08679.x
- ElBasiouny, S. M., Bennett, D. J., and Mushahwar, V. K. (2005). Simulation of dendritic Ca<sub>V</sub> 1.3 channels in cat lumbar motoneurons: spatial distribution. *J. Neurophysiol.* 94, 3961–3974. doi: 10.1152/jn.00391.2005
- Fraser, D. D., and MacVicar, B. A. (1996). Cholinergic-dependent plateau potential in hippocampal CA1 pyramidal neurons. *J. Neurosci.* 16, 4113–4128. doi: 10.1523/JNEUROSCI.16-13-04113.1996
- Gorassini, M., Bennett, D. J., Kiehn, O., Eken, T., and Hultborn, H. (1999). Activation patterns of hindlimb motor units in the awake rat and their relation to motoneuron intrinsic properties. *J. Neurophysiol.* 82, 709–717. doi: 10.1152/jn.1999.82.2.709
- Gorassini, M. A., Bennett, D. J., and Yang, J. F. (1998). Self-sustained firing of human motor units. Neurosci. Lett. 247, 13–16. doi: 10.1016/S0304-3940(98)00277-8
- Grunnet, M., Jespersen, T., and Perrier, J-. F. (2004). 5-HT1A receptors modulate small-conductance Ca2+-activated K+ channels. *J. Neurosci. Res.* 78, 845–854. doi: 10.1002/jnr.20318
- Gustafsson, B., and Pinter, M. J. (1984). Relations among passive electrical properties of lumbar alpha-motoneurones of the cat. *J. Physiol.* 356, 401–431. doi: 10.1113/jphysiol.1984.sp015473
- Harris-Warrick, R. M., Pecchi, E., Drouillas, B., Brocard, F., and Bos, R. (2024). Effect of size on expression of bistability in mouse spinal motoneurons. *J. Neurophysiol.* 131, 577–588. doi: 10.1152/jn.00320.2023
- Harvey, P. J., Li, Y., Li, X., and Bennett, D. J. (2006). Persistent sodium currents and repetitive firing in motoneurons of the sacrocaudal spinal cord of adult rats. *J. Neurophysiol.* 96, 1141–1157. doi: 10.1152/jn.00335.2005
- Heckman, C. J., Johnson, M., Mottram, C., and Schuster, J. (2008). Persistent inward currents in spinal motoneurons and their influence on human motoneuron firing patterns. *Neurosci. Rev. J. Bring. Neurobiol. Neurol. Psychiatry* 14, 264–275. doi: 10.1177/1073858408314986
- Heckman, C. J., Mottram, C., Quinlan, K., Theiss, R., and Schuster, J. (2009). Motoneuron excitability: the importance of neuromodulatory inputs. *Clin. Neurophysiol.* 120, 2040–2054. doi: 10.1016/j.clinph.2009.08.009
- Hivert, B., Bouhanna, S., Diochot, S., Camu, W., Dayanithi, G., Henderson, C. E., et al. (1995). Embryonic rat motoneurons express a functional P-type voltage-dependent calcium channel. *Int. J. Dev. Neurosci.* 13, 429–436. doi: 10.1016/0736-5748(95)00026-D
- Hounsgaard, J., Hultborn, H., Jespersen, B., and Kiehn, O. (1984). Intrinsic membrane properties causing a bistable behaviour of alpha-motoneurones. *Exp. Brain Res.* 55, 391–394. doi: 10.1007/BF00237290
- Hounsgaard, J., Hultborn, H., Jespersen, B., and Kiehn, O. (1988a). Bistability of alpha-motoneurones in the decerebrate cat and in the acute spinal cat after intravenous 5-hydroxytryptophan. *J. Physiol.* 405, 345–367. doi: 10.1113/jphysiol.1988.sp017336
- Hounsgaard, J., and Kiehn, O. (1985). Ca++ dependent bistability induced by serotonin in spinal motoneurons. *Exp. Brain Res.* 57, 422–425. doi: 10.1007/BF00236551
- Hounsgaard, J., and Kiehn, O. (1989). Serotonin-induced bistability of turtle motoneurones caused by a nifedipine-sensitive calcium plateau potential. *J. Physiol.* 414, 265–282. doi: 10.1113/jphysiol.1989.sp017687
- Hounsgaard, J., and Kiehn, O. (1993). Calcium spikes and calcium plateaux evoked by differential polarization in dendrites of turtle motoneurones *in vitro. J. Physiol.* 468, 245–259. doi: 10.1113/jphysiol.1993.sp019769
- Hounsgaard, J., Kiehn, O., and Mintz, I. (1988b). Response properties of motoneurones in a slice preparation of the turtle spinal cord. *J. Physiol.* 398, 575–589. doi: 10.1113/jphysiol.1988.sp017058
- Hounsgaard, J., and Kjaerulff, O. (1992). Ca2+-Mediated plateau potentials in a subpopulation of interneurons in the ventral horn of the turtle spinal cord. *Eur. J. Neurosci.* 4, 183–188. doi: 10.1111/j.1460-9568.1992.tb00865.x
- Hounsgaard, J., and Mintz, I. (1988). Calcium conductance and firing properties of spinal motoneurones in the turtle. *J. Physiol.* 398, 591–603. doi:10.1113/jphysiol.1988.sp017059

- Hultborn, H., Wigström, H., and Wängberg, B. (1975). Prolonged activation of soleus motoneurones following a conditioning train in soleus Ia afferents—A case for a reverberating loop? *Neurosci. Lett.* 1, 147–152. doi: 10.1016/0304-3940(75)90030-0
- Jasinski, P. E., Molkov, Y. I., Shevtsova, N. A., Smith, J. C., and Rybak, I. A. (2013). Sodium and calcium mechanisms of rhythmic bursting in excitatory neural networks of the pre- B ötzinger complex: a computational modelling study. *Eur. J. Neurosci.* 37, 212–230. doi: 10.1111/ejn.12042
- Jeter, R., and Molkov, Y. (2025). Jeterlab/Ionic-Mechanisms-Underlying-Bistability-in-Spinal-Motoneurons (Version Pre-Release) [Computer software]. Zenodo.
- Kernell, D. (1965). The Limits of Firing Frequency in Cat Lumbosacral Motoneurones Possessing Different Time Course of Afterhyperpolarization. *Acta Physiol. Scand.* 65, 87–100. doi: 10.1111/j.1748-1716.1965.tb04252.x
- Kiehn, O., and Eken, T. (1997). Prolonged firing in motor units: evidence of plateau potentials in human motoneurons? *J. Neurophysiol.* 78, 3061–3068. doi: 10.1152/jn.1997.78.6.3061
- Kim, H., and Jones, K. E. (2011). Asymmetric electrotonic coupling between the soma and dendrites alters the bistable firing behaviour of reduced models. *J. Comput. Neurosci.* 30, 659–674. doi: 10.1007/s10827-010-0284-x
- Kuo, J. J., Lee, R. H., Zhang, L., and Heckman, C. J. (2006). Essential role of the persistent sodium current in spike initiation during slowly rising inputs in mouse spinal neurones. *J. Physiol.* 574, 819–834. doi: 10.1113/jphysiol.2006.107094
- Lee, R. H., and Heckman, C. J. (1998a). Bistability in spinal motoneurons *in vivo*: systematic variations in persistent inward currents. *J. Neurophysiol.* 80, 583–593. doi: 10.1152/jn.1998.80.2.583
- Lee, R. H., and Heckman, C. J. (1998b). Bistability in spinal motoneurons *in vivo*: systematic variations in rhythmic firing patterns. *J. Neurophysiol.* 80, 572–582. doi: 10.1152/jn.1998.80.2.572
- Lee, R. H., and Heckman, C. J. (1999). Enhancement of bistability in spinal motoneurons in vivo by the noradrenergic  $\alpha_1$  agonist methoxamine. J. Neurophysiol. 81, 2164–2174. doi: 10.1152/jn.1999.81.5.2164
- Li, Y., and Bennett, D. J. (2003). Persistent sodium and calcium currents cause plateau potentials in motoneurons of chronic spinal rats. *J. Neurophysiol.* 90, 857–869. doi: 10.1152/jn.00236.2003
- Li, Y., Gorassini, M. A., and Bennett, D. J. (2004). Role of persistent sodium and calcium currents in motoneuron firing and spasticity in chronic spinal rats. *J. Neurophysiol.* 91, 767–783. doi: 10.1152/jn.00788.2003
- Morisset, V., and Nagy, F. (1999). Ionic basis for plateau potentials in deep dorsal horn neurons of the rat spinal cord. *J. Neurosci.* 19, 7309–7316. doi: 10.1523/JNEUROSCI.19-17-07309.1999
- Moritz, A. T., Newkirk, G., Powers, R. K., and Binder, M. D. (2007). Facilitation of somatic calcium channels can evoke prolonged tail currents in rat hypoglossal motoneurons. *J. Neurophysiol.* 98, 1042–1047. doi: 10.1152/jn.01294.2006
- Mousa, M. H., and Elbasiouny, S. M. (2020). Dendritic distributions of L-type  $Ca^{2+}$  and  $SK_L$  channels in spinal motoneurons: a simulation study. *J. Neurophysiol.* 124, 1285–1307. doi: 10.1152/jn.00169.2020
- Murray, K. C., Nakae, A., Stephens, M. J., Rank, M., D'Amico, J., Harvey, P. J., et al. (2010). Recovery of motoneuron and locomotor function after spinal cord injury depends on constitutive activity in 5-HT2C receptors. *Nat. Med.* 16, 694–700. doi: 10.1038/nm.2160
- Murray, K. C., Stephens, M. J., Ballou, E. W., Heckman, C. J., and Bennett, D. J. (2011). Motoneuron excitability and muscle spasms are regulated by 5-HT2B and 5-HT2C receptor activity. *J. Neurophysiol.* 105, 731–748. doi: 10.1152/jn.00774.2010
- Olsen, M. L., Campbell, S. C., McFerrin, M. B., Floyd, C. L., and Sontheimer, H. (2010). Spinal cord injury causes a wide-spread, persistent loss of Kir4.1 and glutamate transporter 1: benefit of 17 beta-oestradiol treatment. *Brain J. Neurol.* 133, 1013–1025. doi: 10.1093/brain/awq049
- Perrier, J-. F., and Cotel, F. (2008). Serotonin differentially modulates the intrinsic properties of spinal motoneurons from the adult turtle.  $J.\ Physiol.\ 586,\ 1233-1238.$  doi: 10.1113/jphysiol.2007.145706
- Perrier, J-. F., and Delgado-Lezama, R. (2005). Synaptic release of serotonin induced by stimulation of the raphe nucleus promotes plateau potentials in spinal motoneurons of the adult turtle.  $J.\ Neurosci.\ 25,7993-7999.\ doi: 10.1523/JNEUROSCI.1957-05.2005$

- Perrier, J.- F., and Hounsgaard, J. (2003). 5-HT2 receptors promote plateau potentials in turtle spinal motoneurons by facilitating an L-type calcium current. *J. Neurophysiol.* 89, 954–959. doi: 10.1152/jn.00753.2002
- Phillips, R. S., John, T. T., Koizumi, H., Molkov, Y. I., and Smith, J. C. (2019). Biophysical mechanisms in the mammalian respiratory oscillator re-examined with a new data-driven computational model. *Elife* 8:e41555. doi: 10.7554/eLife.41555.018
- Phillips, R. S., Koizumi, H., Molkov, Y. I., Rubin, J. E., and Smith, J. C. (2022). Predictions and experimental tests of a new biophysical model of the mammalian respiratory oscillator. *Elife* 11:e74762. doi: 10.7554/eLife.74762.sa2
- Picton, L. D., Nascimento, F., Broadhead, M. J., Sillar, K. T., and Miles, G. B. (2017a). Sodium pumps mediate activity-dependent changes in mammalian motor networks. *J. Neurosci.* 37, 906–921. doi: 10.1523/JNEUROSCI.2005-16.2016
- Picton, L. D., Zhang, H., and Sillar, K. T. (2017b). Sodium pump regulation of locomotor control circuits. *J. Neurophysiol.* 118, 1070–1081. doi: 10.1152/jn.00066.2017
- Schadt, J. C., and Barnes, C. D. (1980). Motoneuron membrane changes associated with spinal shock and the Schiff-Sherrington phenomenon. Brain Res. 201, 373–383. doi: 10.1016/0006-8993(80)91041-0
- Schwindt, P. C., and Crill, W. E. (1980). Properties of a persistent inward current in normal and TEA-injected motoneurons. *J. Neurophysiol.* 43, 1700–1724. doi: 10.1152/jn.1980.43.6.1700
- Sharples, S. A., Nisbet, S. J., Broadhead, M. J., Bo Jensen, D., Sorrell, F. L., Meehan, C. F., et al. (2025). Intrinsic mechanisms contributing to the biophysical signature of mouse gamma motoneurons. *J. Physiol.* 0, 1–26. doi: 10.1113/JP289631
- Simon, M., Perrier, J.- F., and Hounsgaard, J. (2003). Subcellular distribution of L-type Ca2+ channels responsible for plateau potentials in motoneurons from the lumbar spinal cord of the turtle. *Eur. J. Neurosci.* 18, 258–266. doi: 10.1046/j.1460-9568.2003.02783.x
- Svirskis, G., and Hounsgaard, J. (1997). Depolarization-induced facilitation of a plateau-generating current in ventral horn neurons in the turtle spinal cord. *J. Neurophysiol.* 78, 1740–1742. doi: 10.1152/jn.1997.78.3.1740
- Tazerart, S., Vinay, L., and Brocard, F. (2008). The persistent sodium current generates pacemaker activities in the central pattern generator for locomotion and regulates the locomotor rhythm. *J. Neurosci.* 28, 8577–8589. doi: 10.1523/JNEUROSCI.1437-08.2008
- Tong, X., Ao, Y., Faas, G. C., Nwaobi, S. E., Xu, J., Haustein, M. D., et al. (2014). Astrocyte Kir4.1 ion channel deficits contribute to neuronal dysfunction in Huntington's disease model mice. *Nat. Neurosci.* 17, 694–703. doi: 10.1038/nn.3691
- Toporikova, N., and Butera, R. J. (2011). Two types of independent bursting mechanisms in inspiratory neurons: an integrative model. *J. Comput. Neurosci.* 30, 515–528. doi: 10.1007/s10827-010-0274-z
- Tysseling, V. M., Klein, D. A., Imhoff-Manuel, R., Manuel, M., Heckman, C. J., Tresch, M. C., et al. (2017). Constitutive activity of 5-HT2C receptors is present after incomplete spinal cord injury but is not modified after chronic SSRI or baclofen treatment. *J. Neurophysiol.* 118, 2944–2952. doi: 10.1152/jn.00190.2017
- Umemiya, M., and Berger, A. J. (1995). Single-channel properties of four calcium channel types in rat motoneurons. *J. Neurosci.* 15, 2218–2224. doi: 10.1523/JNEUROSCI.15-03-02218.1995
- Viana, F., Van den Bosch, L., Missiaen, L., Vandenberghe, W., Droogmans, G., Nilius, B., et al. (1997). Mibefradil (Ro 40-5967) blocks multiple types of voltage-gated calcium channels in cultured rat spinal motoneurones. *Cell Calcium* 22, 299–311. doi: 10.1016/S0143-4160(97)90068-3
- Yan, H-. D., Villalobos, C., and Andrade, R. (2009). TRPC channels mediate a muscarinic receptor-induced afterdepolarization in cerebral cortex. *J. Neurosci.* 29, 10038–10046. doi: 10.1523/JNEUROSCI.1042-09.2009
- Zhang, M., Møller, M., Broman, J., Sukiasyan, N., Wienecke, J., Hultborn, H., et al. (2008). Expression of calcium channel Ca<sub>V</sub> 1.3 in cat spinal cord: light and electron microscopic immunohistochemical study. *J. Compar. Neurol.* 507, 1109–1127. doi: 10.1002/cne.21595
- Zhang, M., Sukiasyan, N., Møller, M., Bezprozvanny, I., Zhang, H., Wienecke, J., et al. (2006). Localization of L-type calcium channel Ca(V)1.3 in cat lumbar spinal cord—With emphasis on motoneurons. *Neurosci. Lett.* 407, 42–47. doi: 10.1016/j.neulet.2006.07.073